UC Berkeley
UC Berkeley Electronic Theses and Dissertations

Title

Urban greenhouse gas emissions from mobile and biogenic sources: An assessment using a high-density sensor network

Permalink

https://escholarship.org/uc/item/6fx2g2sb

Author

Kim, Jinsol

Publication Date

2020

Peer reviewed|Thesis/dissertation

Urban greenhouse gas emissions from mobile and biogenic sources: An assessment using a high-density sensor network

by

Jinsol Kim

A dissertation submitted in partial satisfaction of the

requirements for the degree of

Doctor of Philosophy

in

Earth and Planetary Science

in the

Graduate Division

of the

University of California, Berkeley

Committee in charge:

Professor Ronald C. Cohen, Chair
Professor Inez Y. Fung
Professor Fotina K. Chow

Fall 2020

Urban greenhouse gas emissions from mobile and biogenic sources: An assessment using a
high-density sensor network

Abstract

Urban greenhouse gas emissions from mobile and biogenic sources: An assessment using a high-density sensor network

by

Jinsol Kim

Doctor of Philosophy in Earth and Planetary Science

University of California, Berkeley

Professor Ronald C. Cohen, Chair

The world's cities account for up to 70 % of global carbon dioxide (CO_2) emissions, while covering less than 2 % of the Earth's surface. Achieving global goals of keeping temperature increases below 2°C requires dramatic reductions in emissions. In keeping with this goal, cities around the world are implementing strategies to reduce carbon dioxide emissions. To support this effort, observations and analyses that assess attribution of emission reductions to specific mitigation strategies are needed. However, monitoring and attributing carbon dioxide emissions in cities are challenging since numerous emission sources are densely presented in cities with complex topography and turbulent mixing.

In this dissertation, I present a novel approach to understanding urban carbon dioxide and to attribute emissions to specific source sectors using a near-surface, high-density urban monitoring network. The Berkeley Environmental Air-quality and CO_2 Observation Network (BEACO$_2$N) includes ~70 nodes in the San Francisco Bay Area distributed at ~2 km horizontal spacing. I show that the relationship between CO_2 concentration and highway traffic flow is coherent throughout the network. Using a Gaussian plume model to represent the dispersion from the highways, I show that the observations constrain the decrease in emission rate per vehicle from 2017 to 2019. Increased fuel efficiency and electrification of the vehicle fleet are among the primary tools in California's greenhouse gas reduction plan and this assessment suggest these plans are on track. Second, I leverage the Gaussian plume model to determine biogenic uptake of CO_2 in the region. I find promising estimates of biogenic emissions that is comparable to the daily and seasonal estimates based on SIF. Finally, I describe the implementation and evaluation of other trace gas sensors (O_3, CO, NO, and NO_2) for source attribution. I demonstrate the use of the relationship between trace gases that are co-emitted from combustion to characterize various emission sources.

To my family

Contents

List of Figures

List of Tables

Chapter 1

Introduction

1.1 Motivation and strategies for urban carbon dioxide monitoring

Carbon dioxide (CO_2) is the greenhouse gas (GHG) with the largest contribution to anthropogenic radiative forcing. Consequently, reducing CO_2 emissions is a prime focus for policy aimed at slowing the pace and limiting the ultimate extent of climate change. Anthropogenic emissions have increased CO_2 from 280 ppm in preindustrial times to greater than 400 ppm in the present. There are many ways of looking at controlling CO_2 emissions. Since more than 50 % of the global population lives in urban areas today and the urban population is likely to reach 70 % by 2050, management of CO_2 necessarily must focus on emissions that result from cities. The world's cities account for up to 70 % of global energy-related CO_2 emissions, while occupying less than 2 % of the Earth's surface area (Change et al., 2014). Cities around the world have started implementing mitigation strategies to reduce the CO_2 emissions and collaborating with each other in organizations such as the C40 Cities Climate Leadership Group (https://www.c40.org/) and the Global Covenant of Mayors for Climate and Energy (https://www.globalcovenantofmayors.org/). Cities will manage their emissions both by reducing the emissions that occur directly within their jurisdiction and by reducing the CO_2 emissions they implicitly cause to occur elsewhere by consuming energy, food and material goods. To support urban efforts to reduce emissions within their jurisdictional boundaries, CO_2 monitoring systems are envisioned that can provide direct feedback on the efficacy of policy choices guiding cities toward the most effective CO_2 reduction strategies.

One can begin to understand CO_2 emissions using an activity-based approach to make an estimate of emissions. To do this, source-specific emission factors and the measurements of activities are collected, and the locations of the activities are specified. For example, the mass of CO_2 per mile driven multiplied by the number of miles driven on a specific highway. Uncertainties in activity-based CO_2 emission "inventories" depend on the completeness of

the conceptual model framework and the accuracy of the underlying data and methods used to estimate emissions factors and activity for which direct measures are not available. Source-specific emission factors vary depending on the technology used including engine and post-combustion controls such as catalytic convertors. Activity data used to create these inventories are reported at either national scales or at the scale of smaller jurisdictions that require additional processing such as downscaling. Producing an urban scale CO_2 inventory with hourly resolution and spatial resolution of 1 km or better is thus an extremely labor-intensive process. High spatial resolution activity-based CO_2 inventories have been produced for the cities of Indianapolis, Indiana (Gurney et al., 2012), Paris, France (Bréon et al., 2015), Salt Lake City, Utah (Patarasuk et al., 2016), Los Angeles, California (Gurney et al., 2019), San Francisco Bay Area, California (Turner et al., 2016), and the northeastern region of the United States (Gately and Hutyra, 2017). Recently, a 1 km scale national inventory has been released for cities in the United States (Gurney et al., 2020). It remains to be seen if this national inventory is as effective as inventories that are tailored with local knowledge for specific cities.

A complementary approach to understanding emissions is inferring emissions from CO_2 measurements. Both in situ and remote sensing techniques have been used in this manner. In most cases, observations and a prior inventory such as described above are fused together to yield an improved estimate for an inventory. Methods for fusing the observations include Bayesian inversion, 4-D variational methods and ensemble Kalman filter data assimilation. These approaches all require that a numerical weather model be coupled to emission model with sufficient resolution to resolve variances in the observations.

Spaced-based remote sensing includes the GOSAT, OCO-2 and OCO-3 instruments (Crisp, 2008; Kuze et al., 2009; Eldering et al., 2019). Observations from these instruments were initially used to improve understanding of the global CO_2 cycle (e.g., Chevallier et al., 2007; Liu et al., 2014). More recent attention has turned to the use of these measurements for more localized studies (e.g., Bovensmann et al., 2010; Hedelius et al., 2017, 2018; Kort et al., 2012; Nassar et al., 2017) such as urban enhancements.

Following on the success of the global TCCON network of high resolution sun-tracking column CO_2 observations from the surface, the potential of lower resolution and thus smaller, less expensive and more portable Fourier transform infrared (FTIR) measurements of CO_2 has been developed (e.g., Hedelius et al., 2016; Viatte et al., 2017). These FTIR spectrometers have been deployed for short-term and long-term applications with the sensors analyzed at an upwind site and then a downwind site where the difference in the observed column is interpreted as the accumulation along the path from one to the other. In Los Angeles, California, a novel approach of ground-based Fourier Transform Spectrometer (FTS) that points downwards at 29 different points and provides column measurements along the optical path has been installed (Wong et al., 2015).

Networks of in situ CO_2 instruments have been installed in a number of cities with an eye toward a comprehensive observing and modeling system for assessing CO_2 emissions and trends in the emissions over time. Instrumented cities include Salt Lake City, Utah (Pataki et al., 2005; McKain et al., 2012; Mitchell et al., 2018b), Boston, Massachusetts (Mckain et al., 2015; Sargent et al., 2018), Indianapolis, Indiana (Turnbull et al., 2015; Lauvaux et al., 2016), the San Francisco Bay Area (Shusterman et al., 2016), Los Angeles, California (Verhulst et al., 2017), Baltimore-Washington D.C. (Lopez-Coto et al., 2017), Paris, France (Bréon et al., 2015), Rotterdam, Netherlands (Super et al., 2017b,a). Low-cost CO_2 sensors have also been deployed nationally in Switzerland (Müller et al., 2020).

While the optimal strategy for refining emissions by combining observations with a prior inventory and a chemical transport model is not known, some design principles have emerged. First, the sensitivity of the observations to emissions decays approximately exponentially with distance, thus an increased number of sites spread across the domain of interest generally reduces the uncertainty of estimated emissions (Kort et al., 2013; Staufer et al., 2016; Turner et al., 2016). The cost of instrumentation, along with the labor to maintain instruments and their calibration, has until recently guided most researchers to focus on a modest number of state-of-the-art instruments. The most extensive urban deployments using 0.1 ppm accuracy instruments have ∼15 sites and spacing of order 10 s of km between sites. Recent research has adapted commercially available CO_2 sensors for dense networks with the idea that larger numbers of sensors can capture more of the variation in the atmosphere and that taken as a whole a network of lower cost sensors can provide more accurate constraints on an inverse model than the equivalent capital investment in state-of-the-art measurements. This trade-off between the quality and the quantity of the observations has been investigated by several studies showing that the benefit of higher density exceeds the lower precision of the observations (Lopez-Coto et al., 2017; Turner et al., 2016; Wu et al., 2018).

An advantage of high-density observing systems is their potential to resolve emissions from specific sectors, while previous observational strategies have been more focused on whole-city CO_2 emissions than on sector-by-sector analyses. Turner et al. (2016) showed with a series of observing system simulations that a dense network can resolve localized emissions such as highway emissions. Shusterman et al. (2018) showed that observations from a low-cost, high-density sensor network can provide explicit sensitivity to mobile emissions as the observed CO_2 at every site has a term that is linearly correlated with the total number of vehicles on the roads. Aggregating these observations is expected to allow isolating the transportation sector with sufficient precision to infer annual trends.

1.2 The Berkeley Environmental Air-quality and CO_2 Observation Network

The Berkeley Environmental Air-quality & CO_2 Observation Network (BEACO$_2$N) is a high-density ($\sim 2\,\mathrm{km}$) urban measurement network that began operation in 2013. The current network includes about 75 nodes in San Francisco Bay Area, 20 nodes in Houston and 10 nodes in New York, distributed at approximately $2\,\mathrm{km}$ horizontal spacing. Most of the nodes are deployed on the roofs of schools and museums. Each node is comprised of Vaisala CarboCap GMP343 non-dispersive infrared sensor for CO_2; a Shinyei PPD42NS nephelometric particulate matter sensor; a suite of Alphasense B4 electrochemical sensors for CO, NO, NO_2 and O_3; meteorological sensors for in-node pressure, temperature, dew point temperature and relative humidity. Data collected every $5-10\,\mathrm{s}$ are transmitted via direct on-site Ethernet connection or local Wi-Fi network to a central server, where the data is made publicly available in near-real time (http://beacon.berkeley.edu/). A detailed description of the design and deployment of BEACO$_2$N can be found in Shusterman et al. (2016).

Observations from the distributed network are supplemented by observations from a "supersite" at the Richmond field Station that includes a Picarro G2401 cavity ring-down spectroscopy analyzer measuring CO_2, CH_4, CO, and H_2O; a TSI Optical Particle Sizer 3330 for particulate matter; a Thermo Fisher Scientific 42i-TL NO_X analyzer for NO and NO_2; a Teledyne 703E photometric instrument for O_3; a Pandora spectrometer system for total column O_3 and NO_2; a Lufft CHM 15k ceilometer for cloud and aerosol layer height; and various instruments for meteorological measurements (i.e., a Vaisala WXT520 weather transmitter, a Campbell Scientific CS500 temperature and relative humidity probe, and a Davis 6450 solar radiation sensor).

The CO_2 measurements are calibrated post hoc to yield a bias-corrected dry-air mole fraction. The raw CO_2 concentrations are averaged to $1\,\mathrm{min}$ means and subsequently converted to dry-air mole fraction using site-specific meteorological observations and the ideal gas law. A combination of gradual temporal drift and constant biases or offsets from the true value result in systematic uncertainty for a long-term field deployment that needs to be accounted. This systematic uncertainty is accounted for by reference to the supersite. The data processed through this procedure are estimated to have a precision of $\pm 4\,\mathrm{ppm}$ at $1\,\mathrm{min}$ resolution and $\pm 0.5\,\mathrm{ppm}$ at hourly resolution. The details of the calibration and evaluation of the CO_2 sensor are presented in Shusterman et al. (2016). Updates to account for temperature dependent sensor response have been made and applied to the data used in this dissertation (Delaria, Kim et al., in preparation).

1.3   Research objectives and approach

In this dissertation, my goals are to understand urban carbon dioxide and attribute emissions to specific source sectors. I use a newly developed observing tool, the BEACO$_2$N high-density sensor network, and develop methodologies for application of sensor networks to advancing our understanding of source specific urban emissions.

In Chapter 2, I introduce a novel technique for quantifying traffic emissions. I show that the relationship between CO_2 concentration and highway traffic flow is coherent throughout the network, and that the influence follows a quantitative relationship consistent with Gaussian dispersion: Near highway sites respond strongly to the highway and distant ones less so. The relationships between CO_2 concentration and highway traffic flow at each site are collectively used to infer the average emission rate per vehicle. I compare the three consecutive years of emission rates for the average vehicle and assess prospects for observations to precisely establish rates of decrease from the purchase of more fuel efficient vehicles and to compare that to the goals of California's greenhouse gas reduction plan of $\sim 3\,\%\,\mathrm{yr}^{-1}$ increases in fuel efficiency.

In Chapter 3, I extend this idea to the determination of biogenic uptake of CO_2 in the region. I develop a unique approach to deriving a biogenic CO_2 term. The idea is to attribute the difference between the observed CO_2 enhancement over the background and the mobile term to the biosphere. The biogenic flux is interpreted as the time derivative of this residual term. Comparison of this inference of biogenic emissions with daily and seasonal estimates based on Solar-Induced chlorophyll Fluorescence (SIF) indicate the method is promising. The chapter concludes with discussion of additional research needed to more fully evaluate this approach.

In Chapter 4, I demonstrate the feasibility of using the relationship between trace gases that are co-emitted from combustion to characterize various emission sources. I describe the implementation and evaluation of electrochemical trace gas sensors (O_3, CO, NO, and NO_2) in BEACO$_2$N nodes. Using well-known characteristics of urban air quality and local emissions, I develop a calibration technique that produces observations that can be used in concert with CO_2 to attribute emissions to specific source sectors. Finally, I present the use of the relationship CO_2 and other trace gases to identify the type of emissions and the pattern of specific emissions over space and time.

Chapter 2

Detecting urban CO_2 emissions and trends from the transportation sector

2.1 Introduction

In 2006, California passed Assembly Bill 32 (AB 32), the Global Warming Solutions Act which requires California to reduce its greenhouse gas (GHG) emissions by 40 % from 1990 levels by 2030. Transportation GHG emissions are the largest single category, representing 40 % of the California total. Transportation emissions were 170 MMTCO$_2$e in 2017 (California Air Resources Board, 2017a,b). A steady $3\,\%\,\mathrm{yr}^{-1}$ decrease will yield the state's goal of 103-111 MMTCO$_2$e in the transportation sector by 2030.

In the San Francisco Bay Area, transportation is the largest single source of GHG emissions, again 40 % of the total. The Bay Area Air Quality Management District (BAAQMD) has planned to reduce transportation GHG emissions by a combination of a transition to low and zero emission vehicles, increased reliance on mass transit systems and a reduction of vehicle miles traveled (Bay Area Air Quality Management District, 2017). Vehicle miles traveled (VMT) in 2018 were similar to 2017 (PeMS; http://pems.dot.ca.gov) in the Bay Area. Given the small change in VMT, it seems likely that most of the reduction in vehicle GHG emissions will need to be the result of a decrease in emissions per mile traveled.

Understanding whether these plans are on track will be assessed through a number of economic indicators, such as sales of zero emission vehicles, and sales of gasoline and diesel fuel. In addition, measurements of exhaust plumes can be used in the laboratory using a dynamometer to simulate various driving conditions or in field providing practical emissions of on-road vehicles. On-road approaches include the use of instrumented vans that chase individual vehicles, and a roadside remote-sensing measurements and highway tunnel measurements that provide exhaust emissions for a large sample of vehicles drive by (e.g.,

Dallmann et al., 2013; Bishop et al., 2013; Park et al., 2016; Haugen et al., 2018).

In the last decade, a number of projects have emerged that aim to quantify aspects of urban CO_2 emissions. Projects observing CO_2 in the cities of Indianapolis, Paris, Boston, Salt Lake City, Los Angeles, Baltimore-Washington D.C represent a range of different approaches (Bréon et al., 2015; Lopez-Coto et al., 2017; Mitchell et al., 2018a; Turnbull et al., 2015; Verhulst et al., 2017). Most of these measurements include high accuracy and precision in situ, aircraft and column observations supplementing constrain to activity-based emission inventory. These approaches' focus on city-wide total emissions has led to monitoring strategies that minimize the local signals, thus discarding information from each source/sector.

Instead of total emissions from a city, a densely spaced, lower cost sensor network has been implemented in the San Francisco Bay Area to provide a detailed 1 km map of emissions using formal inversion methods and independently to develop strategies for resolving source/sector specific emissions. Here we describe a novel approach to using dense network observations in a combined analysis to extract the emissions of vehicles from the highways that influence the air in the region sampled by the network. We use observations from the Berkeley Environmental Air quality and CO_2 Observation Network, BEACO$_2$N (Shusterman et al., 2016; Kim et al., 2018) to constrain vehicle emissions during the years $2017-2019$.

In a first analysis of BEACO$_2$N's direct constraints on vehicle related emissions, Shusterman et al. (2018) demonstrated that the CO_2 measurements at each site in the network could be represented by a multiple linear regression with terms that represent local meteorology and a term that is linearly related to the flow of traffic on the nearest highway road segment. The 1σ uncertainty of the proportionality constant relating vehicle flow to CO_2 was found to range from $11-30\%$ at different sites. Leveraging these multiple independent measurements of the response of the atmosphere to the flow of highway traffic in a combined analysis that would gain a square root N advantage was suggested as a route to a higher precision. Simply averaging the different correlation slopes was not an obvious route to producing a more accurate estimate as the slopes are high for sites near the highways and low for sites far from the highways. At the time, no other specific ideas for how to achieve a combined analysis were proposed. If the square root N advantage could be achieved, detection of year over year trends as small as the 3%, which we infer as the state's target for annual decreases in vehicle emissions should be achievable. For example, 25 sites combined would give a 5-fold improvement in precision, yielding an uncertainty of $\sim 2-6\%$.

Here, we propose and evaluate a new approach to integrating all of the network's observations. Our idea builds on a physical model that appropriately recognizes that emission related enhancements are large near a source and decay into a background with distance from that source. We interpret the network's observations by constraining the CO_2 enhancement to follow a Gaussian plume model. While Gaussian plume models have been used to interpret atmospheric dispersion near sources and to infer emission rates directly from observations

Table 2.1: List of site geo-coordinates, height above sea level, relevant traffic monitor IDs, and approximate distances from a highway for 2017 and 2018 Summer, 2018 and 2019 Spring. These periods are when LAN has good data coverage.

Site code	Lat. (°N)	Long. (°E)	Height above sea level (m)	Traffic monitor IDs	Distance from highway (m)
BEL[b,c]	37.775	-122.167	88	400492, 400549	210
BOD[c,d]	37.753	-122.155	82	401857, 401858	300
COL[a,c]	38.002	-122.289	10	400301, 400660	500
CPS[b,c,d]	37.848	-122.240	93	402202, 402480	220
CRP[d]	37.986	-122.308	87	400465, 400838	560
EBM[a,c,d]	37.815	-122.282	4	400093, 400765	1150
				400075, 400815	1360
ELR[d]	37.982	-122.273	38	401230, 401269	1880
ELS[b,c]	37.974	-122.275	129	401230, 401269	2740
FTK[a,c,d]	37.737	-122.174	10	400134, 400955	1350
HRS[a,b,c]	37.809	-122.205	115	402104, 402105	700
LAN	37.794	-122.263	4	400835, 408138	40
LCC[a,d]	37.736	-122.196	4	400740, 400955	220
MAD[a]	37.928	-122.299	207	400819, 401558	1850
OHS[b,c,d]	37.804	-122.237	48	400261, 401017	160
PTL[a,c]	37.920	-122.306	41	400819, 401558	970
SHL[a,c,d]	37.967	-122.298	39	401197, 401243	2030
STW[a]	37.990	-122.291	59	401230, 401269	500

[a] Sites with data available in summer 2017. [b] Sites with data available in summer 2018.
[c] Sites with data available in spring 2018. [d] Sites with data available in spring 2019.

previously (e.g., Choi et al., 2014; Waxman et al., 2019; Varon et al., 2018; Nassar et al., 2017), they have not to our knowledge been used to interpret observations in the context of a sensor network. In this chapter, I explore trends between 2017 and 2019 using the method and make recommendations for further research and refinement of its application.

2.2   Measurements

We use BEACO$_2$N observations from the Spring of 2017 and 2018 and the Summer of 2018 and 2019 (see Fig. 2.1 and Table 2.1). These periods coincide with times when there is good data coverage at the Laney College site (LAN) which is located within 50 m of the highway and is thus especially sensitive to vehicle emissions. Additional details of the design, deployment and evaluation of BEACO$_2$N can be found in Section 1.2. Over the
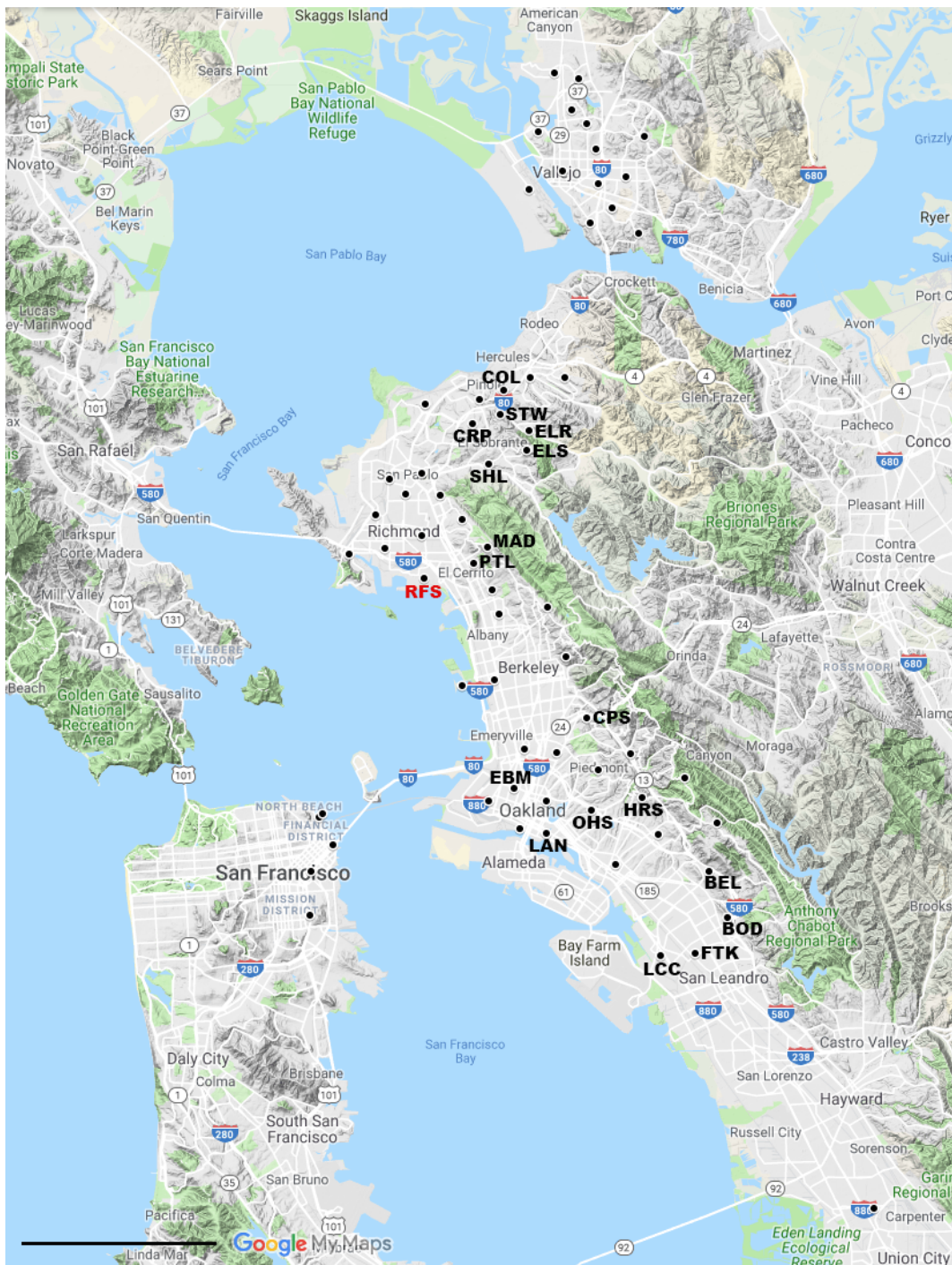
Figure 2.1: Map of San Francisco Bay Area showing BEACO$_2$N node locations (black) and RFS supersite location (red). Nodes used in this study are labeled. Map data ©2019 Google.
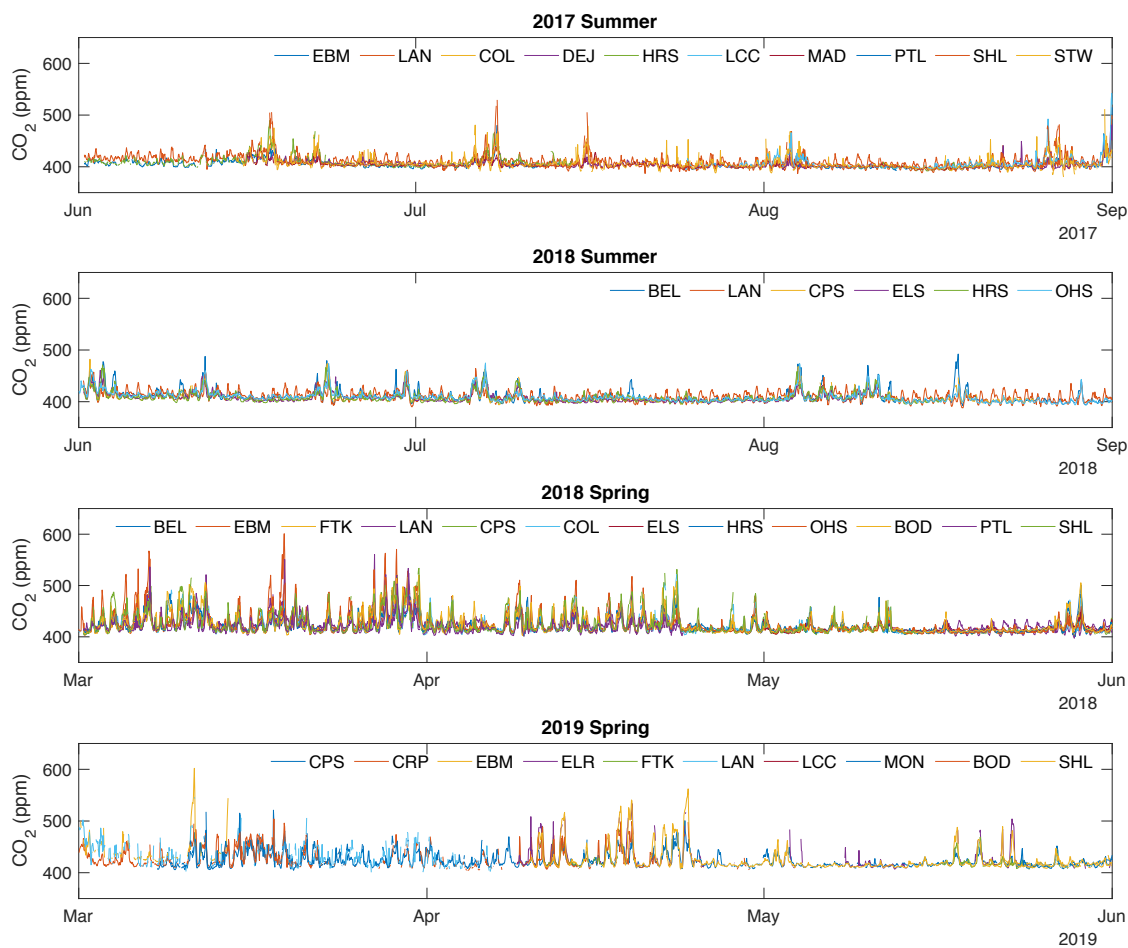
Figure 2.2: Timeseries of CO_2 at the sites available in each season.

years, sites have been added and removed from the network. The network began with ~10 nodes in Alameda county in 2013 has expanded to ~75 locations in four counties including Alameda, Contra Costa, San Francisco, and Solano. The raw 5 s CO_2 concentration at each node was processed into calibrated, bias-corrected, dry-air mole fractions using in-node temperature, pressure and RH observations and in-network reference measurements, and averaged to hourly means. We estimate the uncertainty in the hourly means to be ±0.5 ppm (Shusterman et al., 2016, 2018).

The time series of CO_2 for all the sites used for this analysis are shown in Fig. 2.2. We focus on the portion of the network in and near Oakland and Richmond, CA. Data availability is high and uniform for longer periods immediately following major maintenance of the network in 2017 Summer, 2018 Spring and Summer and 2019 Spring. 17 distinct sites are used in this analysis. There are 10 used in Spring 2017, 6 in Spring 2018, 12 in Summer 2018 and
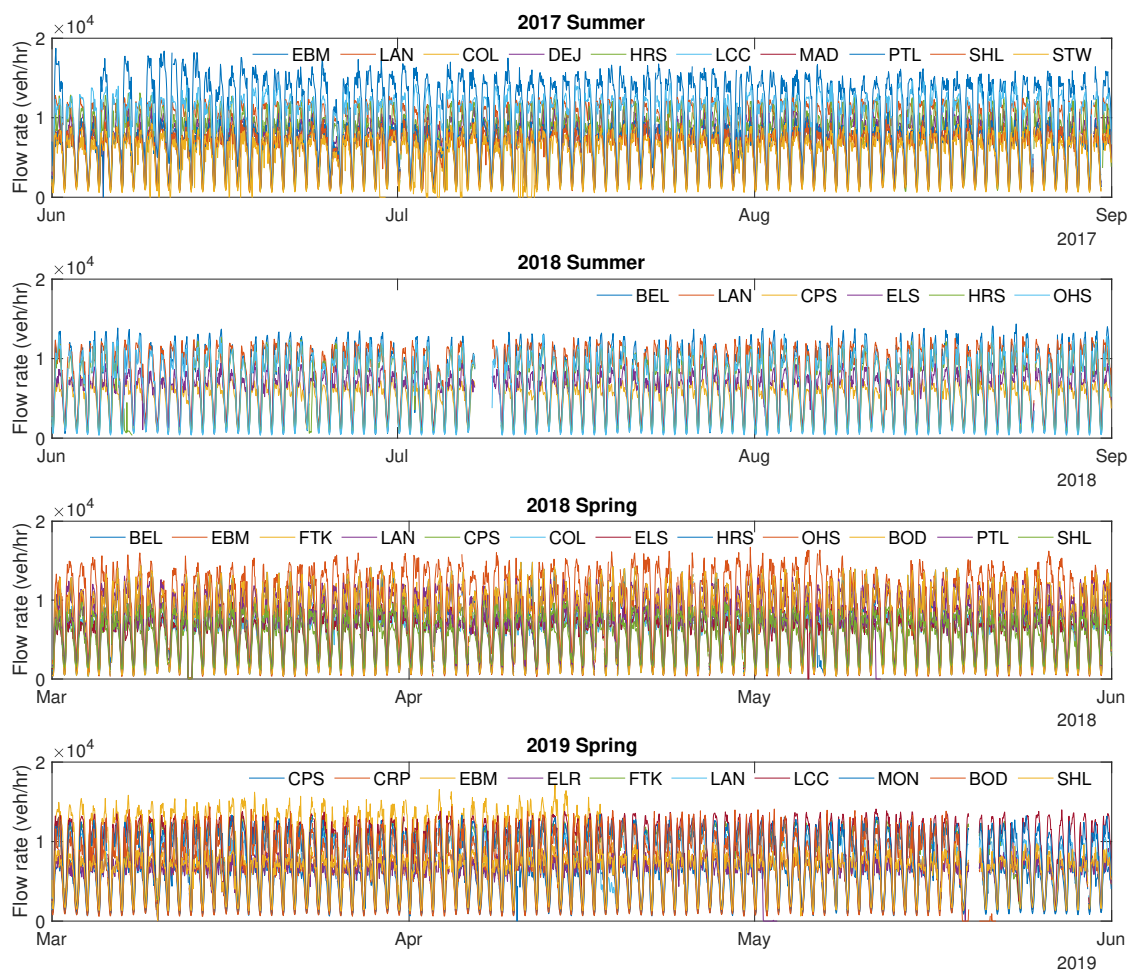
Figure 2.3: Timeseries of vehicle flow rate collected from the monitors to the relevant BEACO$_2$N site.

10 in Summer 2019. Different sites are available in each time period. The Laney college site is the only site that is available in all 4 time periods.

Traffic counts are available through the Caltrans Performance Measurement System (PeMS; http://pems.dot.ca.gov), operated by the California Department of Transportation. Hourly vehicle flow data (in vehicles per hour) and vehicle speed data (in miles per hour) are collected from the monitors at any highway located upwind and closest to the relevant BEACO$_2$N site and summed across all lanes and directions. Only the data with >50 % directly observed, in contrast to modeled, was used. To achieve a complete data set, in some cases monitors upstream or downstream of the desired one was used. The specific monitor IDs used in the analysis are provided in Table 2.1.

Fig. 2.3 shows the time series of vehicle flow rate. Increased traffic is observed during daytime. This diel pattern is superimposed on a weekly pattern showing higher flow rate on weekdays and lower on weekends. Site specific deviations caused by accidents or construction as well as domain wide deviation from routine patterns such as lower traffic flow on Independence Day is also detected.

The lowest values of the observed CO_2 concentrations reflect seasonal variation of the global background with higher values in spring and lower values in summer. Short-term synoptic scale variations, daily variations associated with planetary boundary layer and day-to-day variability caused by local emissions is superimposed on this background. The diel profile of the network-wide CO_2 signal, vehicle flow rate, and PBLH are shown in Fig 2.4. PBLH are taken from the 0.125° by 0.125° resolution ECMWF ERA-Interim model (Dee et al., 2011, http://apps.ecmwf.int/datasets). We see an increase in the CO_2 signal beginning around 04:00 local time (LT), followed by a decrease and then a midday minima. Another increase is observed in early to late evening. This diurnal cycle corresponds well with patterns in traffic emissions superimposed on diel fluctuations in PBLH. Elevated concentrations at night are due to the shallow PBLH and significant enhancements during the morning correspond to the combined effect of shallow PBLH and increased emissions from rush hour traffic. Lower concentrations at midday reflect deeper vertical mixing as PBLH increases after the sunrise.

2.3   Gaussian plume model and emission rate

A Gaussian plume flowing from an infinite line source along the y axis (a highway) with the total reflection at the surface is expressed as

$$C(x, z) = \frac{Q}{\sqrt{2\pi}\,\sigma_z(x)\,U} \left[\exp\left(-\frac{z + H^2}{2\,\sigma_z{}^2(x)}\right) + \exp\left(-\frac{z - H^2}{2\,\sigma_z{}^2(x)}\right)\right] \qquad (2.1)$$

where C [$kgCO_2$ m^{-3}] is the concentration enhancement at the location x, z downwind of the line source, Q [$kgCO_2$ m^{-1} s^{-1}] is an emission rate, U [m s^{-1}] is the wind speed assuming a steady wind oriented along the x axis (perpendicular to the highway), measured from our RFS supersite observation. H [m] is the height of the emission source, and the dispersion parameter σ_z [m] is the standard deviation of the concentration distributed in z direction. Here, we approximate highways in San Francisco Bay Area as infinite line sources on the ground (H=0) and all measurement sites are at the same height (z=0). We treat the BEACO$_2$N sites as if they lie along the x axis (parallel to the wind direction and perpendicular to the line source) to simplify the analysis.

The emission rate Q of the highway line source can be expressed as a product of the emission rate of the average vehicle q [$kgCO_2$ m^{-1} per vehicle] and the flow rate of vehicles (VPS, in vehicles per second):

$$Q = q \times \text{VPS} \qquad (2.2)$$
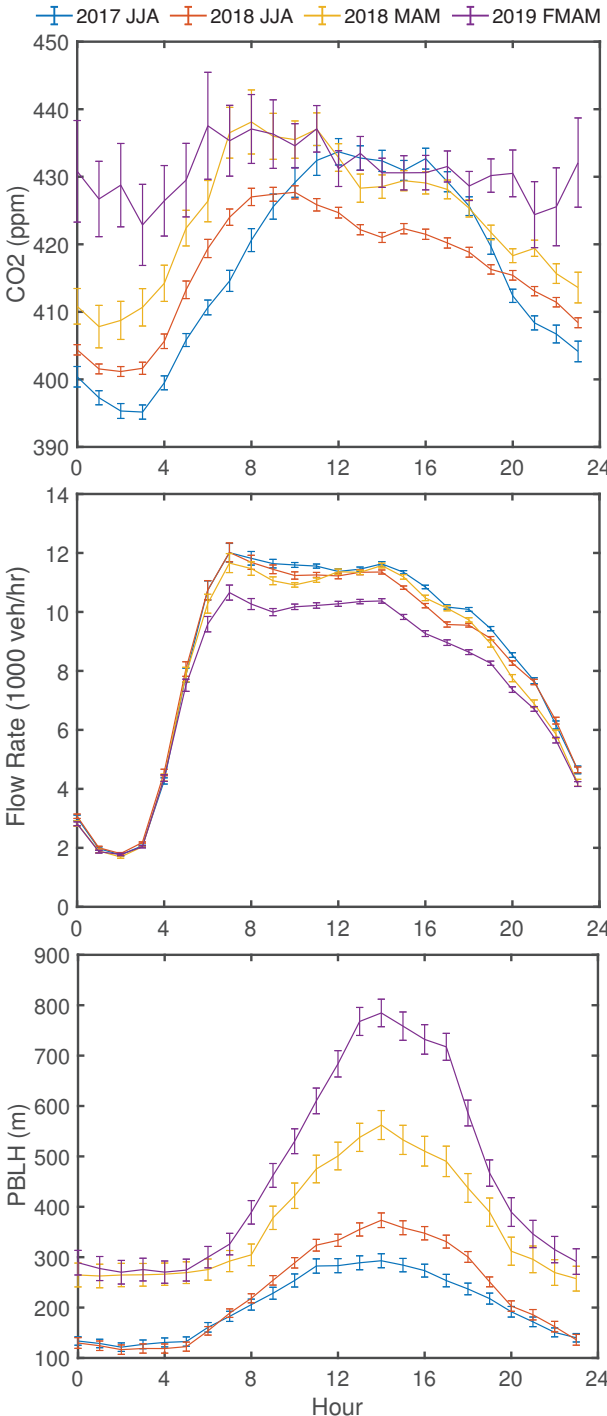
Figure 2.4: Hourly median values of the network-wide (a) CO_2 signals, (b) flow rate from the closest highway, and (c) PBLH. Whiskers indicate standard error of the median.

Applying all the assumptions above and rearranging the emission of the average vehicle q divided by the Gaussian dispersion parameter σ_z simplifies to

$$\frac{q}{\sigma_z(x)} = \frac{\sqrt{2\pi}}{2} \frac{C(x) \cdot U}{\text{VPS}} \tag{2.3}$$

Here, $C(x)$ is the local enhancement of CO_2 due to vehicles traveling on the highway. We define this enhancement as the total enhancement of CO_2 at each location above a single network wide background. The background is defined as the 3-day running mean of the lowest 5th percentile of $BEACO_2N$ observations at all nodes in the network. Since the emission rate of a vehicle q can vary for different traffic conditions, we focus here on the most common mode of traffic, with average vehicle speed faster than 50 mph and exclude times when vehicle speeds are slower than that. For the sites with multiple highways nearby, flow rates from all the highways are integrated assuming a single highway at the distance of average distance from all the highways (see Table 2.1).

Our goal is to derive a self-consistent q that represents the average vehicle on the highways. To do so, we need to estimate the Gaussian dispersion, σ_z. We apply Briggs' formula which is typically used for the dispersion parameterization. The formula differs for rural and urban conditions and with the Pasquill-Gifford stability. Several formulas were tested and no significant difference in the derived q was observed between the stability classes. We adopt the Briggs' formula for urban area at E-F stability (Eq. 2.4) which has the adjustable parameters alpha and beta.

$$\frac{q}{\sigma_z(x)} = \frac{q}{\alpha} \frac{\sqrt{1+\beta x}}{x} \tag{2.4}$$

The dispersion parameter $\sigma_z(x)$ and thus the associated parameters alpha and beta varies with atmospheric conditions, including wind speed, radiation, cloud cover and planetary boundary layer height (PBLH). We assume beta does not vary with these parameters and focus on variations in alpha. Beta is fixed to 0.0015 which is the value Briggs suggests.

$$q/\alpha = \frac{\sqrt{2\pi}}{2} \frac{C(x) \cdot U \cdot \frac{x}{\sqrt{1+\beta x}}}{\text{VPS}} \tag{2.5}$$

Wind speed appears explicitly in equation 2.5. We focus on the other parameter that is the main driver of observed variation, the PBLH. Estimates of PBLH, are taken from the ECMWF ERA-Interim model (Dee et al., 2011, http://apps.ecmwf.int/datasets). We perform a separate analysis at distinct values of PBLH. Dividing the modeled PBLH into 20 quantiles, we assess q/α for each of the PBLH bins using all the sites collectively. The absolute value of α is not well constrained. To assess trends, we compare q/α from the same season and at the same PBLH in different years, assuming alpha is not varying from year to year under similar meteorological conditions.
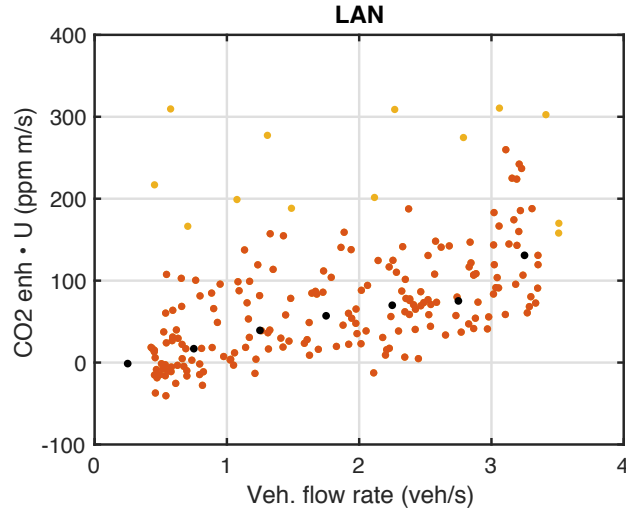
Figure 2.5: CO_2 enhancement multiplied by wind speed at LAN shown as a function of nearby highway vehicle flow rate. 2018 Spring data with PBLH between 100 and 250 m are shown. Black points indicate the median values in each 0.5 vehicles s^{-1} traffic count increment and yellow points indicate outliers defined as 2 standard deviation away from the medians.

2.4   Results and discussion

Figure 2.5 shows the product of the CO_2 enhancement and wind speed (the numerator in Eq. 2.3) vs vehicle flow rate (the denominator in Eq. 2.3) for observations from the Laney College site for PBLH between 100 and 250 m. The slope of the linear regression representing the correlation of these terms at a single location is proportional to $q/\sigma_z(x)$. After removing outliers (shown in yellow), the R-squared for a fit to this data is 0.39. A bootstrap method combined with York regression is used to calculate estimates of the slope $(q/\sigma_z(x))$ for each site located at various distances from the highway.

Values of $q/\sigma_z(x)$ for CO_2 enhancements observed in Spring 2017 and 2018 and summer 2018 and 2019 derived in this manner are shown as a function of distance from the nearest highway in Fig. 2.6. The decrease from large values to near background values occurs within the first 250 m. The functional behavior for a Gaussian plume with q/α=3400 (in 10^{-6} kgCO$_2$ m^{-1} per vehicle) and β=0.0015 is shown in the top panel of figure 2.6. This function is approximately 70 at $x = 50$ m, 10 at 500 m and 3 at 2500 m.

The interpretation of every site as responding to a Gaussian plume originating at the highway assumes that the wind is nominally perpendicular to the highway and the sites are downwind. With this in mind, we see that the sites BAM and SFG (indicated in red in Figure 2.6) which
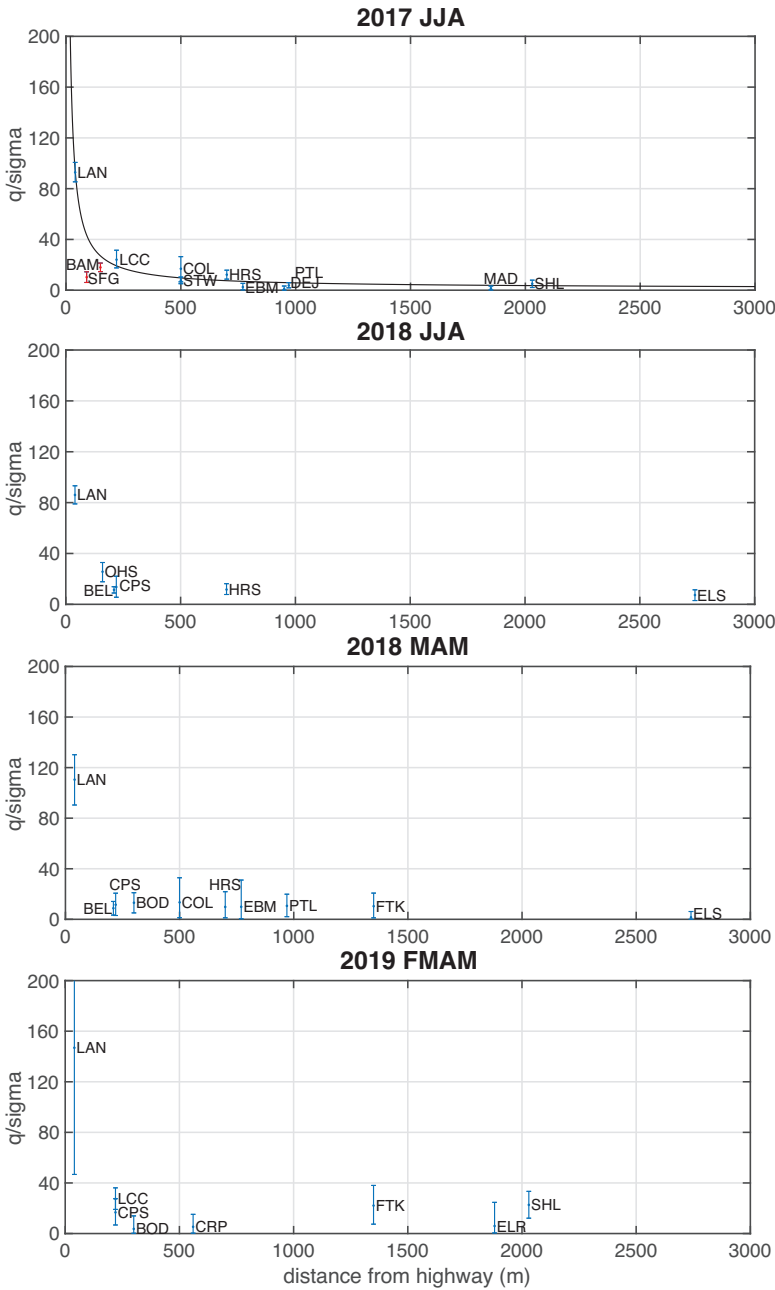
Figure 2.6: Decay of CO_2 signal from highway for PBLH between 100 and 250 m. The functional behavior for a Gaussian plume with q/α=3400 (in 10^{-6} kgCO$_2$ m^{-1} per vehicle) and β=0.0015 (black line) and upwind sites (red) are shown in the top panel as an example. The $q/\sigma_z(x)$ value for each site is plotted with error bars representing the 95 % confidence interval. The confidence intervals were measured by using bootstrap resampling.
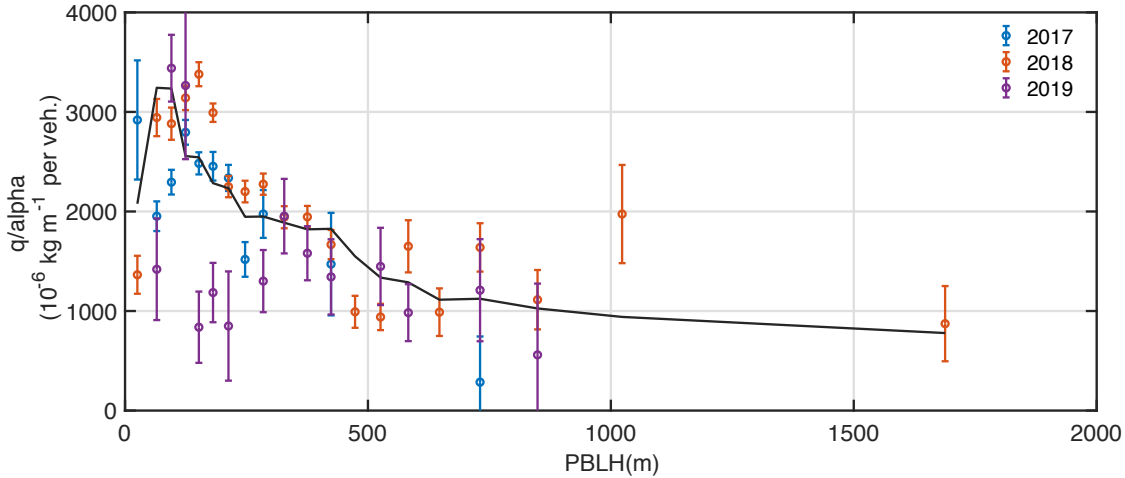
Figure 2.7: q/α for each PBLH quantiles between 2017 and 2019. Error bar represents the standard error of the linear regression performed.

are typically upwind of the highway have $q/\sigma_z(x)$ that is systematically lower than the sites at a similar distance from the highway and thus fall below the predicted Gaussian curve. These sites behave more as if they are far down wind sites than ones close to the highway. This is expected for sites that are predominantly upwind of the nearest highway. We exclude these sites from further analysis. To synthesize observations from all of the sites, we multiply $C(x)$ by $x/\sqrt{1 + \beta x}$ and perform linear regression between $C(x) \cdot U$ scaled with $x/\sqrt{1 + \beta x}$ (the numerator in Eq. 2.5) and vehicle flow rate (the denominator in Eq. 2.5) using data collected from all the sites to calculate q/α for each PBLH quantile. This approach gives more weight to the sites close to the highway which have lower uncertainty in $q/\sigma_z(x)$.

The derived quantity q/α varies strongly with PBLH as shown in Fig. 2.7. If we assume q is invariant with PBLH, then this variation is due to variation in alpha. The largest systematic variation is at low PBLH where the analysis implies small alpha. Larger uncertainty is observed at high PBLH due to relatively fewer data points resulting in wider range bins which are sized to have equal numbers of observations.

While q/α shows an anticorrelation with the PBLH, the relationship is not a clear exponential function (r^2=0.36). By including both PBLH (h) and wind speed (U), the variations in q/α are better explained (r^2=0.56). Wind speed appears in the numerator of both Eq. 2.6 and Eq. 2.5. Thus, the variation with PBLH is the primary phenomenon needed that must drive corresponding variations in alpha or beta. However, it seems to better resolve the variability of CO_2 in San Francisco Bay Area.

$$q/\alpha = \left(1075e^{-0.0032h} + 221\right) \times U \qquad (2.6)$$
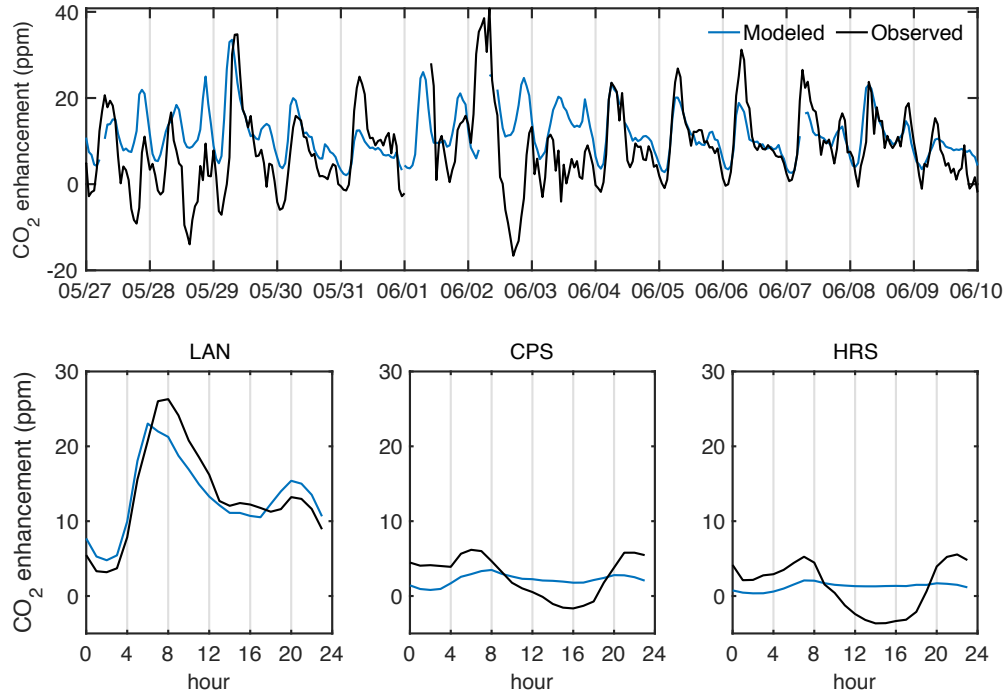
Figure 2.8: Representative 2 week of observed total CO_2 enhancement and modeled traffic CO_2 enhancement at LAN (top), and hourly median values at LAN, CPS, and HRS (bottom).

Combining all of these ideas, we have an equation predicting the CO_2 enhancement caused by mobile sources at any location in the network as a function of VPS, distance from the highway (x), wind speed (U) and PBLH:

$$C(x,t) = \frac{2}{\sqrt{2\pi}} \frac{q\sqrt{1+\beta x}}{\alpha x \cdot U} \text{VPS} \qquad (2.7)$$

Figure 2.8 shows the observed total CO_2 enhancement and modeled traffic CO_2 enhancement at three sites that are 40, 220, and 700 m from the highway. At the site closest to the highway, modeled CO_2 captures the diel variation of observed CO_2 indicating that the mobile emissions are the dominant source. At sites further away, while the morning rush hour enhancements are captured in the modeled CO_2, nighttime values are lower, and daytime values are higher than the observed CO_2. This indicates the influence of other emission sources, such as biosphere, at the sites far from the highway, a signal which will be discussed in chapter 3.

The core result of this analysis is an emission rate per vehicle that is scaled by alpha (q/α) having the uncertainty in the range 3−35 %. For PBLH between 50 and 200 m, q/α is found to be 2880−3380 10^{-6} kgCO$_2$ m^{-1} per vehicle in 2018. For alpha = 0.08, the value provided
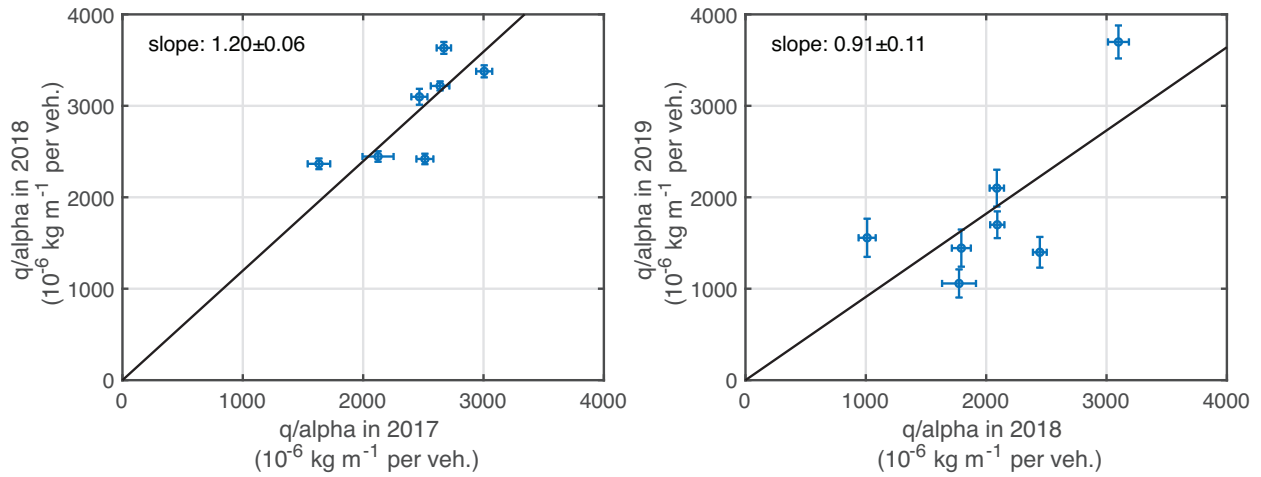
Figure 2.9: Comparison of the values of q/α between 2017 and 2018 (left), and 2018 and 2019 (right). The individual points are comparing q/α for each PBLH quantile shown in Fig. 2.7.

by Briggs' formula for urban area at E-F stability, q is estimated to be $371.05-435.05$ (gCO_2 $mile^{-1}$ per vehicle). This is similar to the mobile emission rate estimated from California Air Resources Board EMFAC2011 model (https://arb.ca.gov/emfac/emissions-inventory) of 389.46 gCO_2 $mile^{-1}$ per vehicle during 2018.

Assuming a specific value for α is not necessary for evaluation of trends if we assume it does not change from year to year. Figure 2.9 compares values of q/α from different pairs of years. The individual points are comparing q/α for each PBLH quantile shown in Fig. 2.7. The fitted line represents the year to year trend. The resulting trend is too large compared to the expected magnitude $\sim 3-5\,\%\,yr^{-1}$.

As we consider the best method for evaluating emission trends, it is useful to compare the results of this manuscript to the analysis of Shusterman et al. (2018) who found precision of the linear coefficient describing the relationship of vehicle flow to CO_2 at $BEACO_2N$ nodes in the range $\sim 10-30\,\%$. Here we have numbers of sites in the range $6-12$ in each year. If a simple square root N scaling in precision was appropriate, we would expect to have precision in the relationships developed in this paper that are $2-3$ times better, putting them in the range $3-15\,\%$. We do find this overall improvement at an individual PBLH. However, when we use all of the PBLH values we do not find consistency and the overall uncertainty in a comparison of two consecutive years rises to $\sim 10\,\%$. This indicates that there is a systematic bias that needs to be identified.
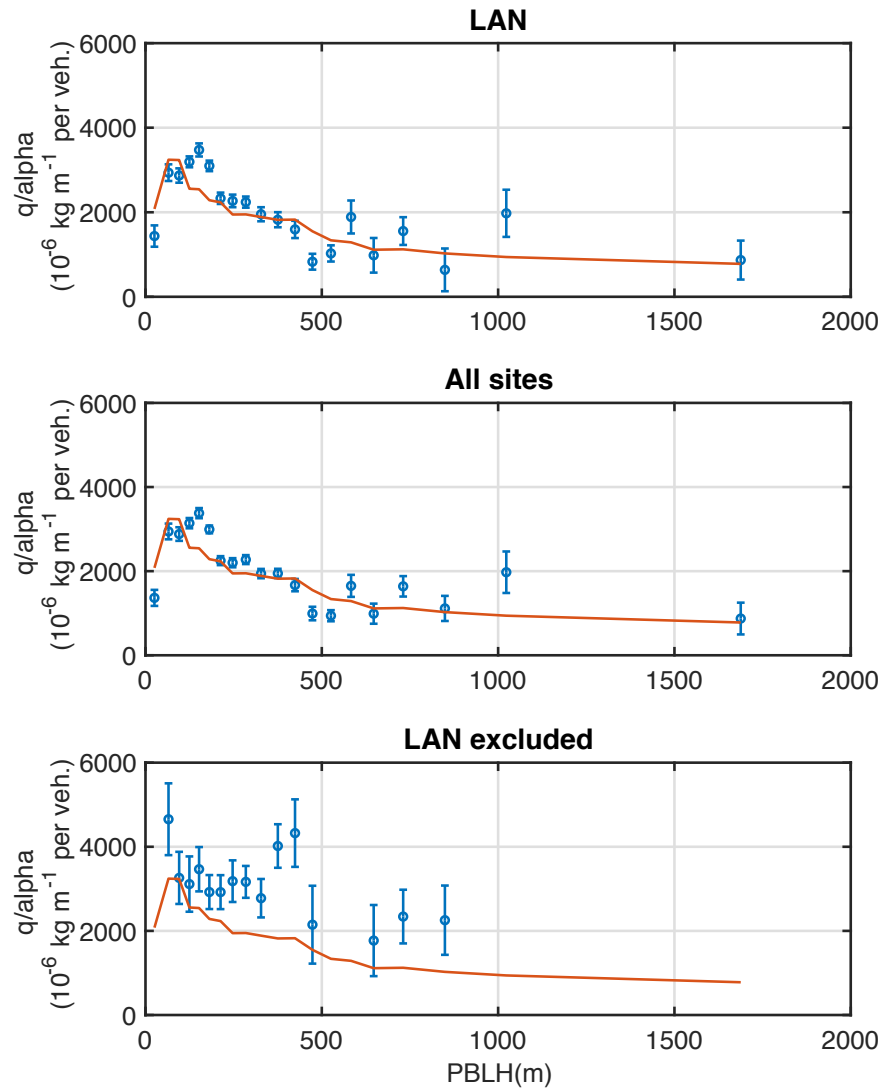
Figure 2.10: q/α estimated for 2018. Top panel is showing estimations using LAN, middle panel is using all available sites, and bottom panel is using all the sites except LAN.

Several distinct factors are at play in these overall uncertainty estimates. First, the use of two different wind speed measurements, NOAA measurements from the Port of Oakland International Airport (http://www.ncdc.noaa.gov/isd/) for 2017 and our more frequent measurements at RFS in 2018 and 2019 introduces a potential bias. Second, the Laney college site which is within 40 m of the highway has an out-sized influence on the analysis, one that would be mitigated with larger numbers of sites included in the analysis or adding other near highway locations to the network. In periods where there is comparatively less LAN data, especially in 2019, the uncertainty in the derived emission rate is much larger than

the other years analyzed (see Fig. 2.7). The latter factor is exhibited in Figure 2.10 where the estimated emission rate using LAN alone (top panel), is compared to the emission rate estimated using all the sites (middle panel), and all the sites except LAN (bottom panel). The uncertainty of the estimated emission rate using LAN alone is nearly identical to the estimation using all the sites.

The use of a Gaussian plume model is associated with several assumptions that contribute to our uncertainty in estimation of emission rate. The Gaussian plume formula is calculating the steady-state concentration. We assume the emission rate is constant within an hour and that steady-state concentrations are reflected in our hourly measurements. We assume the wind speed is constant and unidirectional and treat the $BEACO_2N$ sites as if they lie along the wind flow. Errors in observed and model variables, the influence of other local emissions and the assumption listed above introduces uncertainty in the estimation of emission rate. We define and remove outliers in the process of calculating $q/\sigma_z(x)$ for each site (see Fig. 2.5) to reduce the uncertainty. The dispersion parameter $\sigma_z(x)$ and the associated parameters alpha and beta varies with atmospheric conditions (see Eq. 2.4). We assume beta does not vary and alpha varies with PBLH. This parameterization also contributes to the uncertainty in derived quantities.

While there is much promise in this approach, it is not yet sufficient to meet our goal of detecting trends of order $3\,\%\,yr^{-1}$ in vehicle emissions. To reduce the uncertainty enabling to track even smaller reduction in the emission rate per vehicles, I recommend the following additional steps: use more sites in the analysis, especially more sites close to the highways, use longer time periods of the analysis, develop a more explicit analysis of the role of PBLH, use wind direction data more explicitly to account for the true distance and upwind/downwind status of each site relative to its highway line source and perhaps also self consistently remove the influence of other sources. As figure 2.8 shows, the influence of other sources is large compared to the traffic influence at the downwind sites likely adding considerable noise to the determination of the traffic related emissions. Another approach would be to combine the constraints from CO and CO_2. As emission factors of CO and CO_2 varies for different sources, it should be a powerful additional constraint.

2.5 Conclusions

We have presented and evaluated a conceptual model based on Gaussian plumes to detect year to year trends in CO_2 emission rates by vehicles on highways. We take advantage of CO_2 measurements from a high-density urban monitoring network by leveraging a large number of sites at a range of distances from highway sources. The precision of fits to individual sites presented by Shusterman et al. (2018) was $11-30\,\%$. Here we find we are able to produce a precision of order $10\,\%\,yr^{-1}$. This level of precision for the emission factor for a single sector of emissions has not yet been demonstrated in any other previous studies.

While the analysis does not yet meet our goal of measuring year over year change with a precision of $3\,\%\ \mathrm{yr}^{-1}$, there are many promising features of the approach that suggest with further refinement it will achieve that goal. To achieve this goal, first, more sites near the source as well as more sites overall in the analysis and longer time periods of the analysis are recommended. Second, a more explicit approach to account for vertical mixing, advection along the wind relative to its highway line source would improve the precision. Last, self consistently removing the influence of other sources by leveraging an additional tracer, such as CO that can provide unique signature for each different source, would achieve even greater confidence.

Chapter 3

Contribution of biogenic sources to urban CO_2 variation

3.1   Introduction

While CO_2 emissions in cities are primarily associated with fossil fuel combustion, even in the densest cities CO_2 variations are also affected by biological activity. Recent analyses of urban CO_2 suggest that biogenic emissions and uptake are comparable to fossil fuel fluxes, especially during the growing season. By incorporating atmospheric transport models and biospheric models, Sargent et al. (2018) and Vogel et al. (2019) have shown that for Boston and Paris biogenic uptake is a major influence on daily CO_2 variations. Lauvaux et al. (2020) has shown that biogenic uptake is the dominant feature of the CO_2 budget in Indianapolis and that the urban fossil fuel signal can be accurately determined if this biogenic background is adequately characterized.

Observational methods for separating the role of biogenic and anthropogenic CO_2 emissions often rely on radiocarbon using the fact that fossil fuels are completely depleted in ^{14}C. Measurements of ^{14}C, provided at time scales of weekly to monthly, allows quantifying seasonal variations in biogenic and fossil contributions (e.g., Djuricin et al., 2010; Miller et al., 2012; Pataki et al., 2003). Another approach uses the correlation of CO_2 with the incomplete combustion product carbon monoxide (CO) that can be measured continuously. However, initial studies suggest this approach is not as effective because of variance in the CO/CO_2 ratio (e.g., Djuricin et al., 2010; Newman et al., 2013; Turnbull et al., 2006). These prior analyses are limited to quantifying relative contribution to observed CO_2 variations.

Previous studies have used urban monitoring networks that typically consist of 2-15 high-quality instruments attempting to constrain domain-wide emissions (Bréon et al., 2015; Lopez-Coto et al., 2017; Mitchell et al., 2018a; Turnbull et al., 2015; Verhulst et al., 2017).

These networks focus on the biosphere as an external control on the background CO_2 and not as an integral part of the net urban CO_2 flux. Here we describe a novel approach to using dense observation network to derive biogenic emissions. Understanding processes affecting urban biogenic activities will lead to a better understanding of the net urban CO_2 flux.

We propose and present an initial evaluation of a method that enables characterizing daily variation in biogenic emissions within the boundaries of a dense urban network. The idea is unique. We begin with a characterization of the diel pattern of the CO_2 enhancement at each site in the BEACO$_2$N network. Then we assess the anthropogenic CO_2 attributable to traffic emissions at each site, decomposing the observed CO_2 enhancement into a traffic and a biogenic term, assuming that other CO_2 sources are negligible. We evaluate the contribution of the biosphere to CO_2 fluxes in the BEACO$_2$N domain and describe their variation on daily and seasonal scales. We are not aware of any other analysis of CO_2 concentrations that is capable of identifying seasonal variations in biospheric uptake within the urban domain without application of a land-use or other biospheric model. The ability we develop here to describe biogenic CO_2 emissions and uptake on a fine spatial and temporal scale using a high-density sensor network will enhance our understanding of processes affecting urban biogenic fluxes.

3.2 Methodology

3.2.1 Observations from the Berkeley Environmental Air-quality and CO_2 observation Network

We use San Francisco Bay Area CO_2 observations from BEACO$_2$N during the spring and summer of 2018 (see Fig. 3.1 and Table 3.1). A detailed description of design, deployment and evaluation of BEACO$_2$N can be found in Section 1.2. Briefly, about 75 nodes are densely distributed in the area at approximately 2 km horizontal spacing. Collected raw CO_2 measurements are processed into dry-air mole fractions, corrected for systematic bias as described in Sect. 1.2, and averaged to hourly means. A time series of six representative sites for the full period from March to September 2018 is shown in Fig. 3.2 along with two examples of one week of observations at these six sites taken from March and June. The short-term variability caused by local and regional emissions is superimposed on day-to-day synoptic scale variations and a seasonal variation that follows the trend of global background with a maximum in May and minimum in September.

3.2.2 Gaussian plume model and dispersion

The Gaussian plume model for an infinite line source has been discussed in Chapter 2. Briefly, assuming highways in San Francisco Bay Area are an infinite line source (along the y axis) on the ground, and all the site are on the ground along the wind direction (following
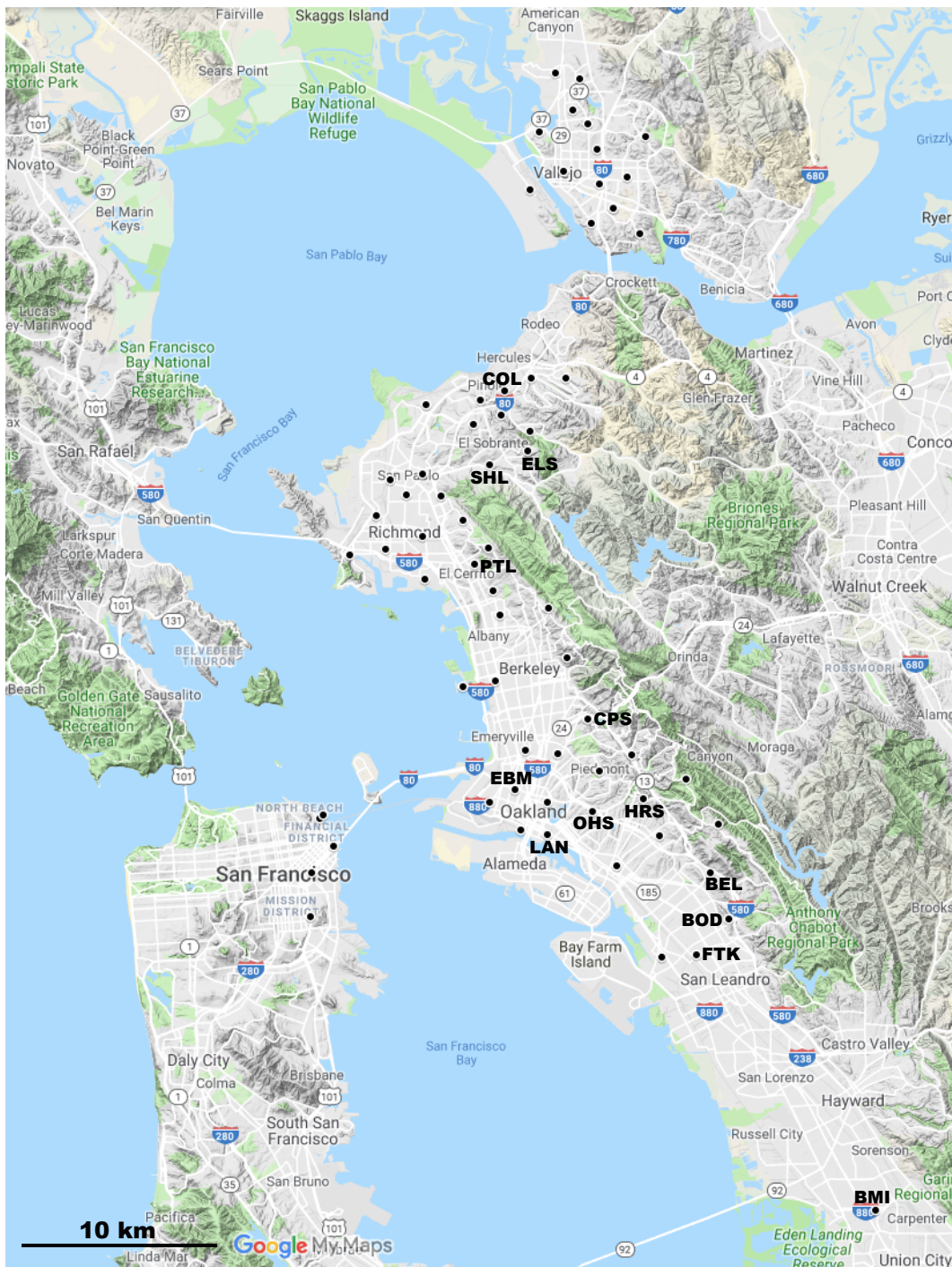
Figure 3.1: Map of San Francisco Bay Area showing BEACO$_2$N node locations in black. Nodes used in this study are labeled. Map data ©2019 Google.

Table 3.1: List of site geo-coordinates, height above sea level, relevant traffic monitor IDs, and approximate distances from a highway for spring and summer of 2018.

Site code	Lat. (°N)	Long. (°E)	Height above sea level (m)	Traffic monitor IDs	Distance from highway (m)
BEL	37.775	-122.167	88	400492, 400549	210
BOD[a]	37.753	-122.155	82	401857, 401858	300
COL[b]	38.002	-122.289	10	400301, 400660	500
CPS	37.848	-122.240	93	402202, 402480	220
EBM[a]	37.815	-122.282	4	400093, 400765	1150
				400075, 400815	1360
ELS	37.974	-122.275	129	401230, 401269	2740
FTK[a]	37.737	-122.174	10	400134, 400955	1350
HRS	37.809	-122.205	115	402104, 402105	700
LAN	37.794	-122.263	4	400835, 408138	40
OHS	37.804	-122.237	48	400261, 401017	160
PTL[a]	37.920	-122.306	41	400819, 401558	970
SHL[a]	37.967	-122.298	39	401197, 401243	2030

[a] Sites with data available in spring 2018 only. [b] Sites with data available in summer 2018 only.

x axis and perpendicular to the line source), the Gaussian plume equation can be expressed as

$$C(x,t) = \frac{2}{\sqrt{2\pi}} \frac{q\sqrt{1+\beta x}}{\alpha x \cdot U} \text{VPS} \tag{3.1}$$

In Chapter 2, we detail how we apply this approximation to the BEACO$_2$N data to derive q/α from Gaussian plume analysis using 12 available sites collectively:

$$q/\alpha = \frac{\sqrt{2\pi}}{2} \frac{C(x) \cdot U}{\text{VPS}} \frac{x}{\sqrt{1+\beta x}} \tag{3.2}$$

C [kgCO$_2$ m^{-3}] is the concentration enhancement at the location x, U [m s^{-1}] is the wind speed assuming a steady wind oriented along the x axis (perpendicular to the highway), measured from our RFS supersite observation, and VPS is the flow rate of vehicles [vehicles per second]. q [kgCO$_2$ m^{-1} per vehicle] is emission rate of the average vehicle, and alpha and beta are dimensionless dispersion coefficients.

The dispersion parameter σ_z and the associated parameters alpha and beta are a function that varies with different atmospheric conditions. We find the two most important terms are wind speed and the planetary boundary layer height (PBLH) and parameterize it with the two terms:

$$q/\alpha = \left(1075e^{-0.0032h} + 221\right) \times U \tag{3.3}$$
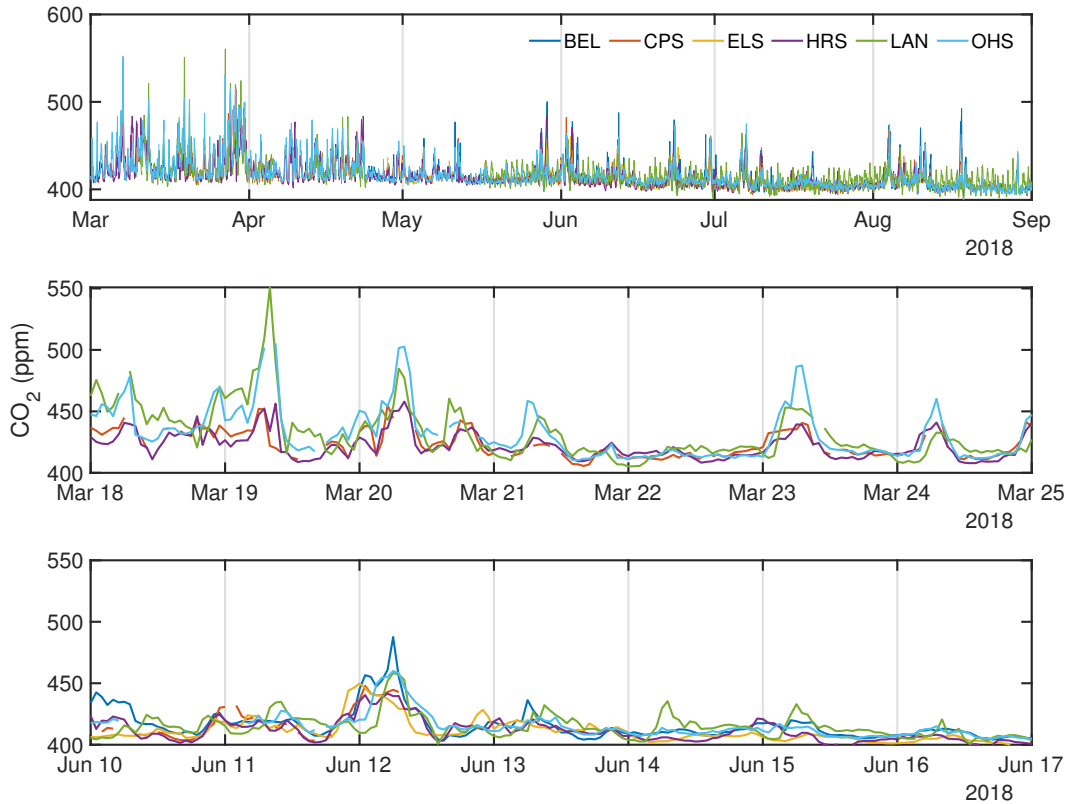
Figure 3.2: Time series at six representative sites from March to September (top). 1 week-long time series in Spring (middle) and in Summer (bottom). Hourly CO_2 measurements are demonstrated.

Here, h is boundary layer height (in m), U is wind speed (in m s^{-1}), and average CO_2 emission per vehicle q is a fixed constant. Mobile CO_2 enhancement can be predicted using Eq. (3.1 and 3.3) as shown in Chapter 2.

3.2.3 Estimating mobile and biogenic emission fluxes

The CO_2 emission inventory for the region is estimated to have 3 large terms. The mobile source term and the biosphere are known to have large daily variations that are out of phase. Industrial sources are assumed to be constant in time, and home heating and other anthropogenic sources are assumed to be small. Figure 3.3 shows predictions from the inventory developed by Turner et al. (2016, 2020a). In this inventory, more than 80 % of the emissions that are not vehicular or biogenic are industrial point sources. The 10 highest point source emitters account for more than 70 % of the emissions and 3 of them are located in the BEACO$_2$N domain. These are refineries that are thought to operate 24/7 with no diurnal variation in their emissions. In this analysis, we assume signals from these point sources
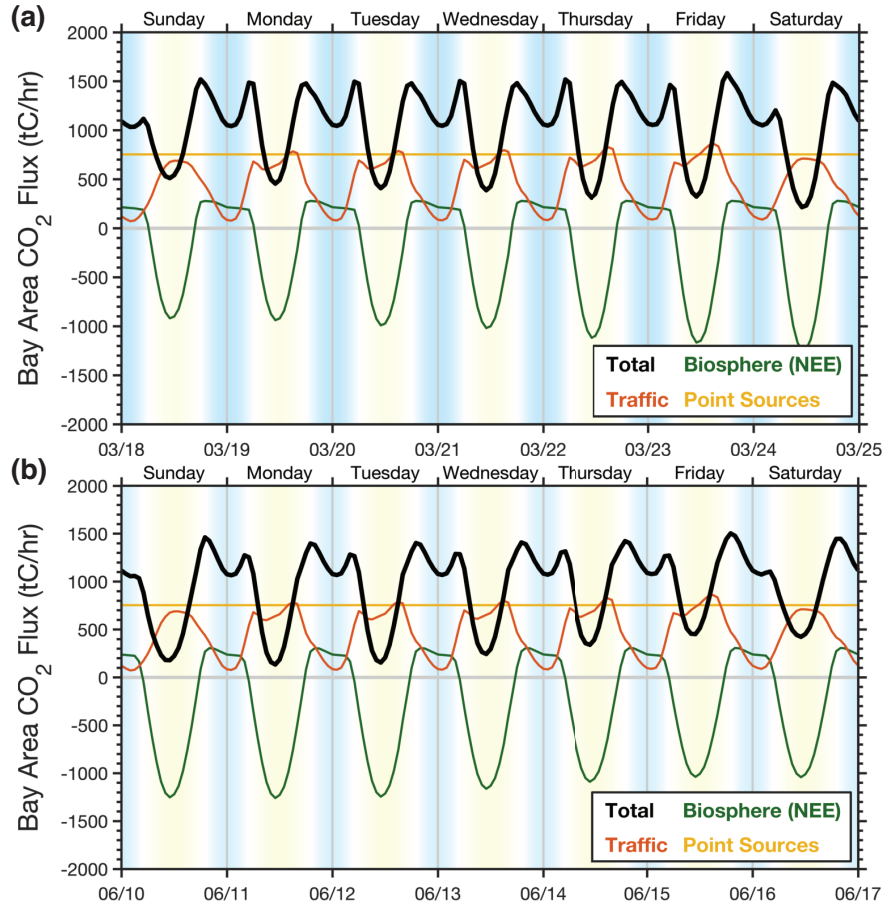
Figure 3.3: Representative week-long time series of Bay Area CO_2 emission inventory for (a) Spring and (b) Summer.

are detected only occasionally since the plume of an industrial point source is expected to be narrow, inferred from the empirically derived range of the dispersion parameter σ_y and σ_z. With this assumption, we decompose observed CO_2 enhancement above the background into a biogenic emission and a mobile source emission term.

For each hour, at each site, we use the measured vehicle flow at the nearest highway segment from the Caltrans Performance Measurement System (PeMS; http://pems.dot.ca.gov), the measured wind speed from our RFS supersite observation, and Gaussian dispersion parameter σ_z defined in Chapter 2. With these parameters, we calculate the CO_2 enhancement due to mobile emissions at each site in the network using Eq. 3.1.

After subtracting the vehicle CO_2, we attribute the residual to biogenic signal and derive the time derivative of this biogenic term. This time derivative term represents overall emission
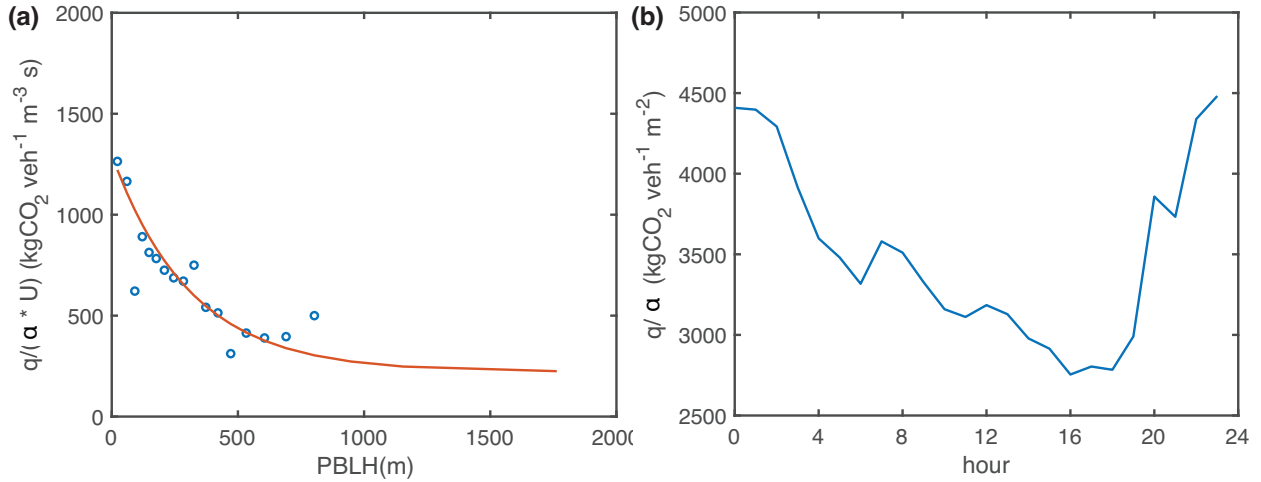
Figure 3.4: (a) $q/\alpha \cdot U$ for each PBLH quantile. Fitting line of Eq. 3.2 is shown in red line. (b) Diel pattern of q/α.

detected in a representative grid, which is shown to be approximately $2\,\text{km}$ in the $BEACO_2N$ domain (Shusterman et al., 2018). Overall emissions include not only local sources, but also regional sources that are transported and detected at the measurement site. Assuming that $BEACO_2N$ nodes are deployed in every grid of the whole domain, the sum of the time derivative of the biogenic term from each grid point gives the total emissions over the region of influence. By dividing this time derivative term in $\text{kg}\,\text{m}^{-3}\,\text{s}^{-1}$ with boundary layer height, we obtain emission flux in $\text{kg}\,\text{m}^{-2}\,\text{s}^{-1}$ over the region of the $BEACO_2N$ footprint.

3.3 Results and discussion

3.3.1 The diel cycle of mobile and biogenic CO_2 signals

As a summary of Chapter 2, here we show the relationship between $q/\alpha \cdot U$ and PBLH in Fig. 3.4a. This implies that sigma is a strong function of PBLH. The red line in Fig. 3.4a indicated the parameterized q/α and Fig. 3.4b demonstrates the median diel cycles of modeled q/α predicted from PBLH and wind speed. q/α is higher at night corresponding to stable conditions and low wind speeds. q/α is lower during the day reflecting unstable conditions and higher wind speeds. Urban turbulent mixing at nighttime is found to be 2/3 of daytime in San Francisco Bay Area. This relationship between turbulent mixing and time of day deserves further research to assess how accurately it is reflected in the inferred CO_2 emissions.
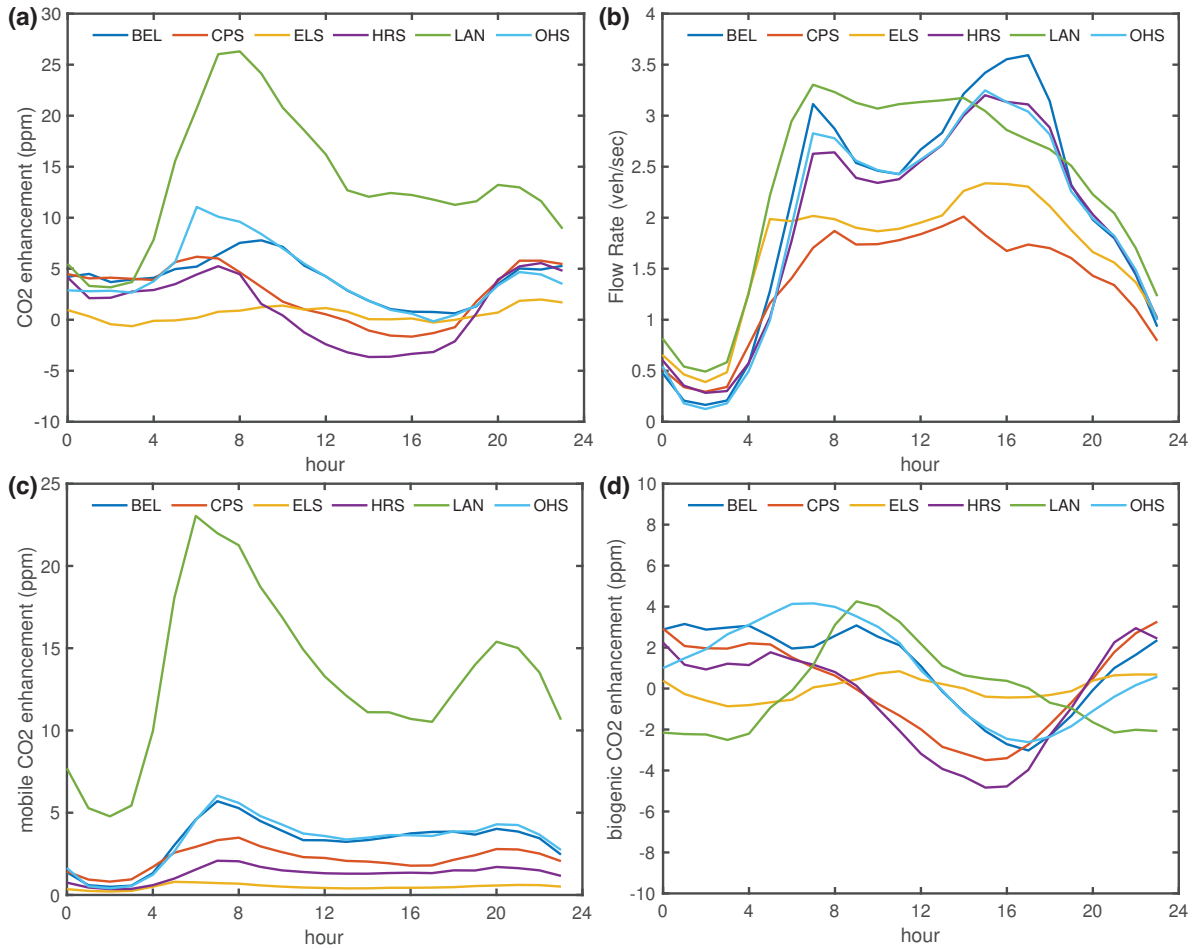
Figure 3.5: Diel cycle of (a) CO_2 enhancement, (b) vehicle flow rate, (c) predicted mobile CO_2 enhancement, and (d) biogenic CO_2 enhancement at six representative sites.

Observed median diel cycles are shown in Fig. 3.5. In general, we see a typical diel cycle of CO_2 revealing higher concentration at night corresponding to emissions into a shallow nocturnal boundary layer (lower α) and lower concentrations during the day reflecting deep mixing layer (higher α), even though emissions are larger during the day. These indicate that understanding the diel cycle of mixing dynamics is crucial to understanding the diel variations in observed CO_2 from an in-situ measurements. Additional tracers, such as ^{222}Rn that are consistently emitted without a short-term scale variation, to track the dynamics of mixing would offer opportunities to better understand the urban boundary layer and its effects on observed CO_2.
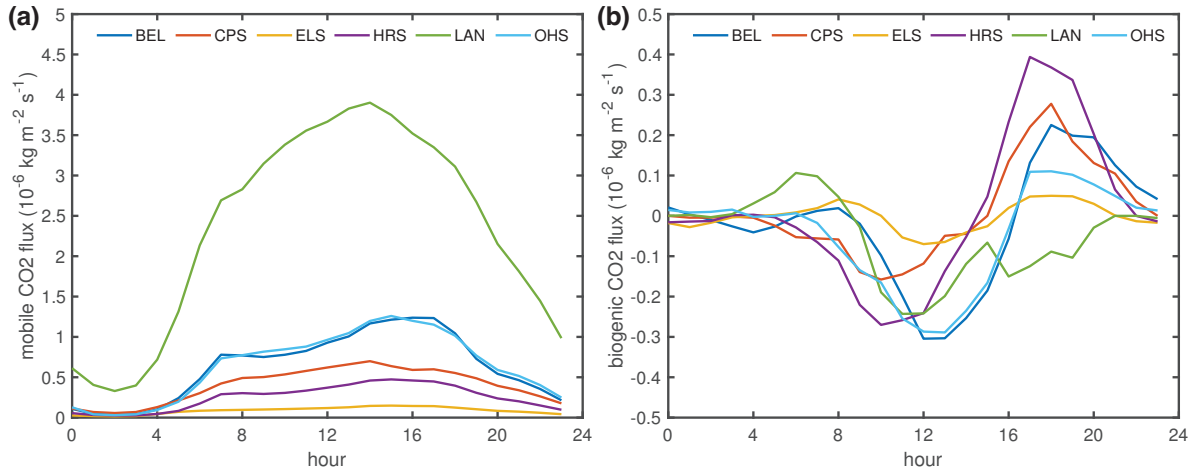
Figure 3.6: Diel pattern of (a) estimated mobile CO_2 flux and (b) biogenic CO_2 flux.

Using the predicted q/α (see Fig. 3.4) and the measured vehicle flow rate (see Fig. 3.5b), we calculate the CO_2 enhancement due to mobile emissions at each site in the network using Eq. 3.1. The diel cycle of mobile CO_2 enhancement predicted using the Eq. 3.1 and 3.3 is shown in Fig. 3.5c. Mobile CO_2 signals at LAN is elevated compared to the other sites due to its proximity to the highway (40m). The magnitude of the mobile CO_2 signals indicates each site's distance to the highway. The residual CO_2 enhancement is shown in Fig. 3.5d. In general, positive enhancement is observed at nighttime and negative enhancement at daytime representing biogenic CO_2 signals. At LAN, overestimation of mobile CO_2 enhancement at nighttime and underestimation at daytime results in an opposite pattern in the residual enhancement.

3.3.2   Contribution of mobile and biogenic emissions

In this section we describe the inferred biogenic emissions from the BEACO$_2$N network and compare the inferred emissions to expectations and to other observations. The diel pattern of the derived mobile CO_2 fluxes for the six example BEACO$_2$N nodes is shown in Fig. 3.6a. CO_2 is emitted more during the daytime compared to the nighttime and some of the sites show peaks in the morning and evening rush hours corresponding well with the observed vehicle flow rate pattern (see Fig. 3.3b).

Fig. 3.6b shows the estimated CO_2 fluxes from the biosphere for these same six nodes. The biogenic fluxes are negative near local noon, which represents the peak of photosynthesis. While BEL and HRS have strong negative fluxes around noon, CPS and ELS show weaker fluxes that do not peak at noon. These differences represent the spatial heterogeneity that is the main objective of our dense sensor network, BEACO$_2$N. We believe they record local
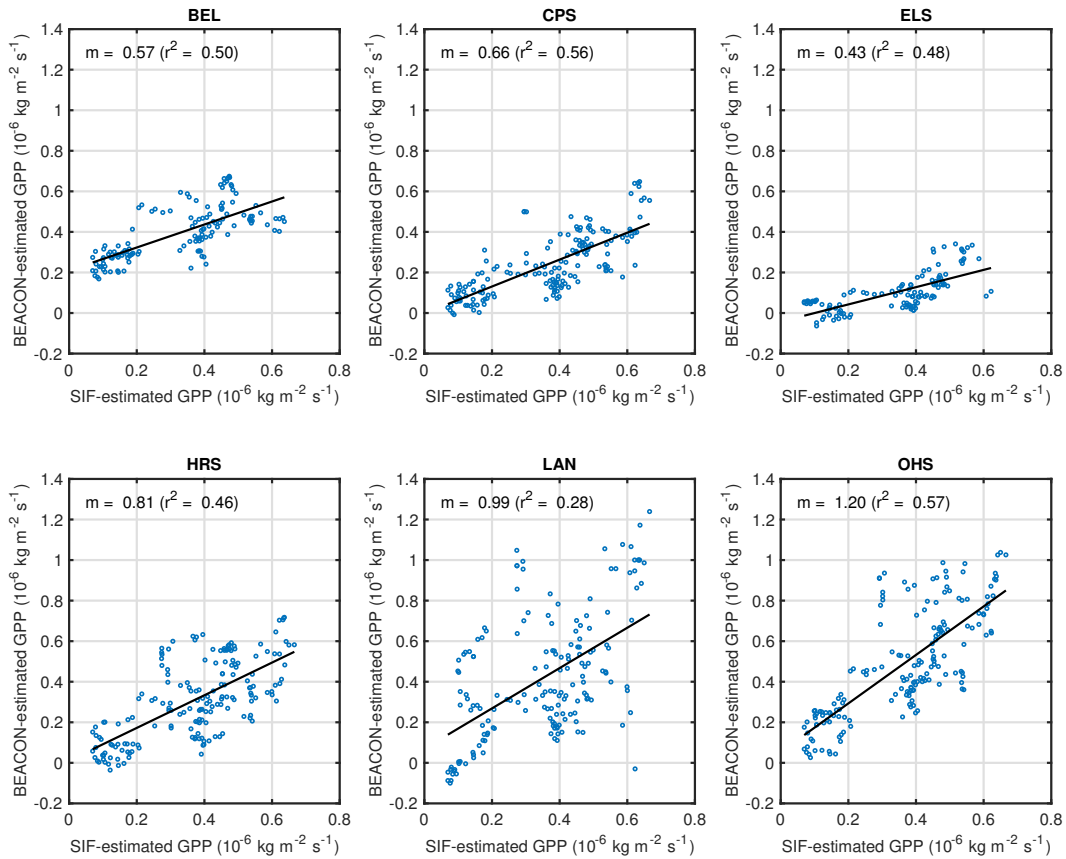
Figure 3.7: Comparison of estimated GPP with GPP estimated from SIF data at each site. BEACO$_2$N-based GPP was calculated for time between 13:00 and 14:00 PST, similar to the TROPOMI overpass time at 13:30, and smoothed with a moving 14-day window, same as the SIF data. SIF-based GPP was estimated using the linear relationship reported by Turner et al. (2020b) and averaged over the San Francisco Bay Area.

differences in biogenic emissions. Further analysis with sites that are distributed across a broader domain, including sites that are near and far from local biospheric influence, will provide additional insight into the biogenic processes influencing spatially variant urban CO_2. The biogenic fluxes are near zero in the period from midnight to 6AM and in the afternoon at half of the sites. However, three of the sites exhibit large positive fluxes. We speculate that these results are from an underestimate of the vehicle flux at a time of rapid change in the PBLH (see Fig. 3.5c and 3.6a) caused by the systematic bias in vehicle flow rate and parameterized mixing dynamics using PBLH. But they might also be due to breakdown of other assumptions such as our assumption that other area sources (e.g., driving on city streets, home heating and human respiration) are negligible.

Net ecosystem exchange (NEE; CO_2 fluxes) can be separated into gross primary productivity (GPP; CO_2 uptake) and total ecosystem respiration (R; CO_2 release). The CO_2 flux at night is equivalent to R which is expected to be $15-20\%$ of the CO_2 flux near local noon (Turner et al., 2020a). CO_2 flux near local noon is the sum of GPP and R which is shown to be $0.2-0.3$ ($10^{-6}\,\mathrm{kg\,m^{-2}\,s^{-1}}$) in fig 3.6b, inferring R to be in the range of $0.03-0.06$ ($10^{-6}\,\mathrm{kg\,m^{-2}\,s^{-1}}$). If this assumption of 10% R is correct, the BEACO$_2$N estimates of CO_2 fluxes are approximately equal to GPP. Fig 3.7 compares the estimated biogenic uptake at six sites, where data is available in both spring and summer, to the regional average estimate of biogenic CO_2 uptake based on the TROPOMI Solar-Induced chlorophyll Fluorescence (SIF) data that has been shown to have linear relationship with GPP (Turner et al., 2020b). BEACO$_2$N-based GPP was calculated for time between 13:00 and 14:00 PST, similar to the TROPOMI overpass time at 13:30, and smoothed with a moving 14-day window, to match the SIF data. We find a strong correlation between GPP estimated from BEACO$_2$N and SIF with slopes in the range $0.43-1.20$ and $r^2 = 0.5-0.6$ except for the Laney site where the r^2 is $\sim$0.3. We use root mean square error of the linear regression which is due to the combined random errors in the SIF and BEACO$_2$N based measures of biogenic flux and the estimated noise of the SIF retrieval of GPP of 0.07 ($10^{-6}\,\mathrm{kg\,m^{-2}\,s^{-1}}$), to derive an estimate of the 1σ uncertainty in the BEACO$_2$N-based GPP of 0.1 ($10^{-6}\,\mathrm{kg\,m^{-2}\,s^{-1}}$).

Fig 3.8a show the average of network-wide, estimated biogenic emissions at 13:30 PST. Site LAN, which has large uncertainty in estimated biogenic emissions, has been excluded. Some of the seasonal variability in the BEACO$_2$N biogenic CO_2 estimate is remarkably similar to the variability inferred from the SIF. For example, both decrease from mid-April to mid-May and again during July. This correspondence is suggestive that the methods developed in this Chapter are capturing some of the key elements of regional biogenic emissions. In spring, higher variability is observed compared to summer. This variability pattern can be explained by the higher variations in PBLH and wind speed in spring and nearly constant pattern in summer as we use these two variables to parameterize the mixing behavior.

Fig 3.8 compares the estimated mobile and biogenic emissions. The emission rate of vehicle CO_2 is about 0.75 ($10^{-6}\,\mathrm{kg\,m^{-2}\,s^{-1}}$) in March and 0.60 ($10^{-6}\,\mathrm{kg\,m^{-2}\,s^{-1}}$) in August. The correspondence between this estimate of emissions from mobile sources and the vehicle flow rate drifts by about 5% over the 6 months shown (lower at the end of the record). The estimated flux into the biosphere begins at 0.5 ($10^{-6}\,\mathrm{kg\,m^{-2}\,s^{-1}}$) in March, a value equal to 2/3 of the vehicle emission rate. It decreases to about 0.15 ($10^{-6}\,\mathrm{kg\,m^{-2}\,s^{-1}}$) which is $\sim$25 % of the vehicle emissions in August.

BEACO$_2$N observations start in 2013 providing a long-term record of CO_2 in the region. Future analysis of these long-term CO_2 observations will evaluate the feasibility to capture the interannual trends in biogenic emissions. For example, 2018/19 winter season was wet compared to 2017/18 and 2019/20. The difference in biogenic activity caused by this pattern should affect the BEACO$_2$N observations. High-density observation tool, BEACO$_2$N, should
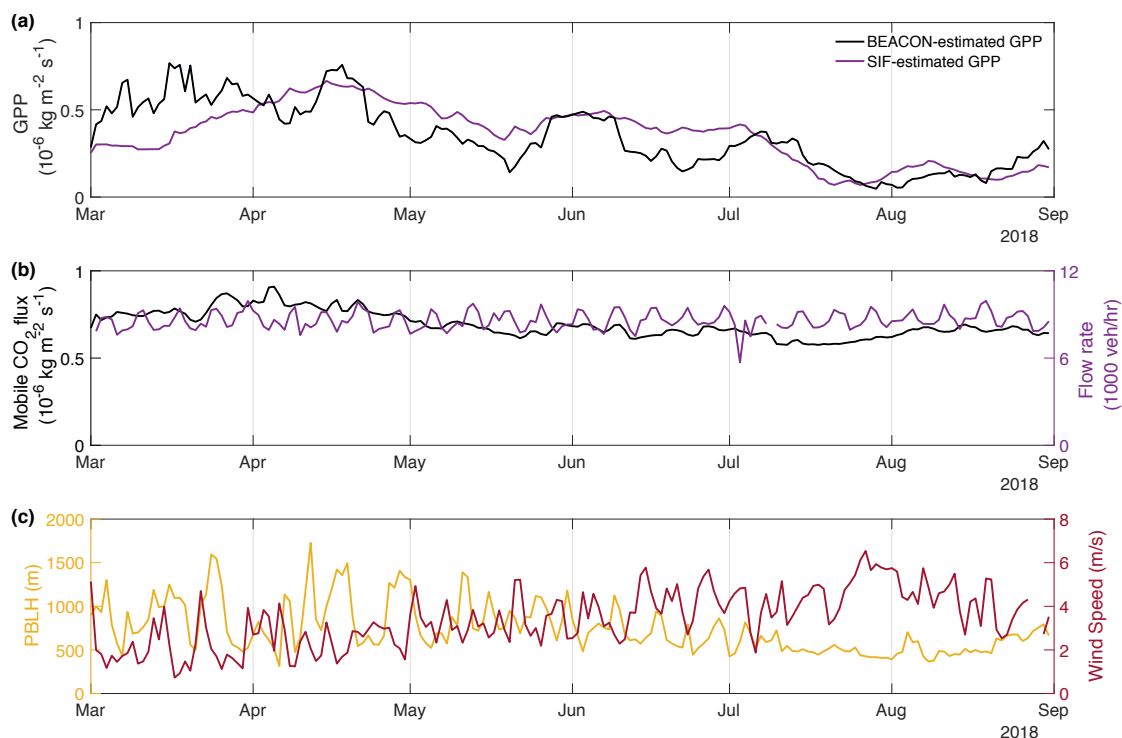
Figure 3.8: (a) Spatial average of estimated GPP and regional average of GPP estimated from SIF data. (b) Spatial average of mobile CO_2 flux and the flow rate. Mobile and biogenic fluxes are average of data between 13:00 and 14:00 PST and smoothed with a moving 14-day window. (c) Daily maximum PBLH from the ERA-Interim Reanalysis and daily average wind speed measured at $BEACO_2N$ supersite.

also resolve the spatial pattern of urban biogenic fluxes providing better understanding of where the flux is coming from. Instead of considering biogenic flux as an external control on background CO_2, urban biogenic activity within the city limits can be assessed directly using this method.

3.4   Conclusions

We have presented a novel approach to deriving biogenic emissions rates from a newly developed observing tool, the $BEACO_2N$ dense network. The method produces regional scale fluxes directly from the ambient CO_2 measurements enabling to study the effect of biogenic activities on urban CO_2 variation without the use of biospheric or chemical transport models. A high degree of correspondence to CO_2 uptake inferred from SIF is observed. This comparison lends confidence to the approach and suggests further development and evaluation of the method to detect finer time scales of daily to longer time scales of inter-annual

variability will be a productive line of research. The ability we develop here to describe biogenic CO_2 emissions and uptake on a fine spatial and temporal scale using a high-density sensor network will enhance our understanding of processes affecting urban biogenic fluxes.

Chapter 4

Characterizing urban emission sources using relationships between co-emitted trace gases

4.1   Introduction

CO_2 emissions from fossil fuel combustion are the main source of the postindustrial increase in atmospheric CO_2 concentration and urban areas account for up to 70% of global energy-related CO_2 emissions (Change et al., 2014). Cities around the world have already started implementing mitigation strategies to reduce fossil fuel CO_2 emissions. At the same time, emissions of gases and particles that contribute to poor air quality are often associated with combustion of fossil fuels. Treating these emissions and other measurements as additional atmospheric tracers is useful for separately quantifying distinct the emission sources (e.g., Miller et al., 2012; Nathan et al., 2018; Turnbull et al., 2011).

For example, radiocarbon (^{14}C) is useful to distinguish fossil fuel CO_2 sources from biogenic and other CO_2 sources. However, ^{14}C cannot further partition fossil fuel emissions into source sectors. Some studies have suggested using other tracers together with ^{14}C to get source information (e.g., Djuricin et al., 2010; Newman et al., 2016). The stable isotope ^{13}C can be used to separate emissions from gasoline and natural gas (Pataki et al., 2003, 2006). These isotope methods require sample collection, preparation and analysis which limits the number of measurements. In contrast, carbon monoxide (CO) is a widely used tracer that

can be measured continuously (e.g., Djuricin et al., 2010; Newman et al., 2013; Turnbull et al., 2006). CO is co-emitted with CO_2 during incomplete combustion and the ratio varies depending on the carbon content of the fuel and combustion conditions.

Conventional approaches to monitoring trace gases rely on a limited number of relatively high cost instruments that lack the spatial resolution needed to characterize specific emission activities at neighborhood scales. To resolve individual emission sources, much higher spatial resolution is needed. One approach to obtaining finer spatial resolution observations is passive sampling, which has been implemented using inexpensive sampling devices that can be later analyzed in bulk. Passive samplers do not require electrical power to function properly and are collected and analyzed one to two weeks after deployment. Such protocols provide high spatial resolution but also have significant drawbacks. Spatial resolution is gained at the expense of temporal resolution, and analysis after collection of the samplers is time consuming, thus passive sampling has typically been used only in short duration experiments (e.g., Krupa and Legge, 2000; Cox, 2003). Furthermore, as a result of boundary layer dynamics, passive sampling in urban areas is likely dominated by the high concentrations found at night and relatively insensitive to daytime variability.

Recent developments in low-cost sensors for trace gases and particulate matter, as well as advances in software and hardware enabling low-cost data communication, have made high-density, high time resolution monitoring possible for trace gases. Devices and networks of devices are emerging that are low cost, report at a time resolution of seconds, and are capable of long-term deployment, providing potential for improvement over the two major weaknesses of passive sampling. Examples include metal oxide sensors used to measure O_3, CO, NO_2, and total VOCs (e.g., Williams et al., 2013; Bart et al., 2014; Piedrahita et al., 2014; Moltchanov et al., 2015; Sadighi et al., 2018), and electrochemical sensors used to measure CO, NO, NO_2, O_3, and SO_2 (e.g., Mead et al., 2013; Sun et al., 2015; Jiao et al., 2016; Hagan et al., 2018; Jerrett et al., 2017; Mueller et al., 2017). These different low-cost sensor systems have been evaluated and compared (e.g., Borrego et al., 2016; Papapostolou et al., 2017).

Here we propose monitoring other trace gases as well as CO_2 at high spatial resolution to characterize individual emission sources. The Berkeley Environmental Air-quality & CO_2 Observation Network (BEACO$_2$N) is a low-cost, high-density greenhouse gas (CO_2) and air quality (CO, NO, NO_2, O_3, and particulate matter) monitoring network. Other trace gases are measured not only for air quality monitoring, but also for attributing urban emission sources. BEACO$_2$N consists of approximately 70 "nodes," deployed with approximately 2 km horizontal spacing in San Francisco Bay Area, California (see Fig 4.1). This high spatial resolution monitoring is achieved by using a suite of low-cost trace gas sensors.

We begin by describing laboratory experiments and in-field comparisons to co-located reference instruments that give an initial characterization of the sensors and provide insight
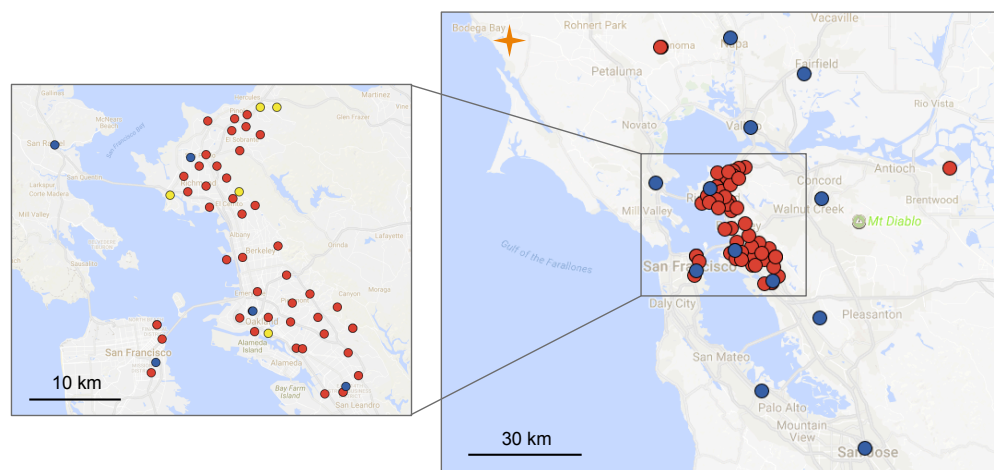
Figure 4.1: Map of San Francisco Bay Area showing current BEACO$_2$N node sites (red), BAAQMD reference sites with O$_3$ measurements (blue), and the BAAQMD Bodega Bay regional greenhouse gas background site (orange). The sites plotted in Fig 4.7 are marked in yellow on the detailed panel.

into the effects of temperature, humidity, and cross-sensitivity to non-target analytes. Then we describe an in-situ calibration strategy that accounts for this challenge without investing considerable time and labor. Finally, we evaluate the air quality monitoring network against regulatory quality measurements and provide examples of using relationships between co-emitted trace gases to characterize urban emission sources.

4.2   Instrument Description

Details of the node design and deployment are described in Shusterman et al. (2016). Briefly, each BEACO$_2$N node contains a Vaisala CarboCap GMP343 non-dispersive infrared sensor for CO$_2$, a Shinyei PPD42NS nephelometric particulate matter sensor, and a suite of Alphasense electrochemical sensors: CO-B4, NO-B4, either NO$_2$-B42F or NO$_2$-B43F, and either Ox-B421 or Ox-B431. All sensors are assembled into compact, weatherproof enclosures as shown in Fig. 4.2. Two 30 mm fans are located on either side of the enclosure to facilitate airflow through the node. A Raspberry Pi microprocessor collects data via a serial-to-USB converter for CO$_2$ and an Adafruit Metro Mini microcontroller for all other sensors. Then, data collected every 5 or 10 s is transmitted to a central server using a direct on-site Ethernet connection or a local Wi-Fi network.

The Alphasense B4 electrochemical gas sensing series that we use employs a four-electrode approach. The electrodes are embedded in an electrolyte solution separated from the atmo-
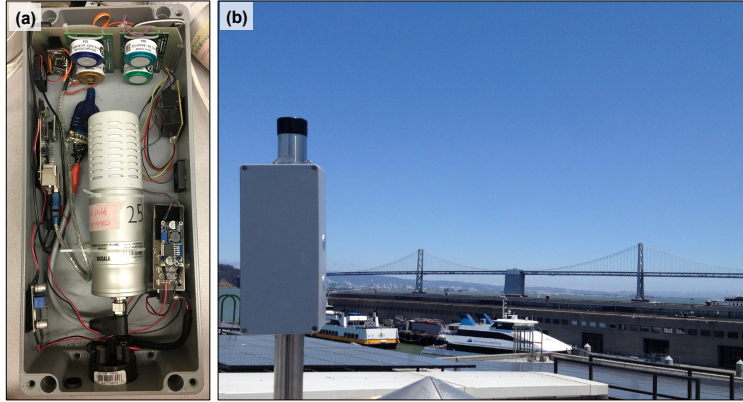
Figure 4.2: (a) Current BEACO$_2$N node design and (b) a photo of a node deployed.

sphere by a semi-permeable membrane. The gas of interest diffuses through the membrane into the electrolyte where it contacts a "working" electrode, and is either oxidized (in the case of NO and CO) or reduced (NO$_2$ and O$_3$). The potential at the working electrode is maintained at a constant value with respect to a "reference" electrode. Electric charge produced at the working electrode is balanced by the complementary redox reaction at a "counter" electrode, generating an electric current. The sensor also contains an "auxiliary" electrode, which shares the working electrode's catalyst structure, but is isolated from the ambient environment, accounting for fluctuations in the background current associated with other processes at the electrode and electrolyte. Subtracting the auxiliary current from the working current gives a corrected current dependent on the gas concentration.

The working and auxiliary currents detected by the sensors are converted to working and auxiliary voltages using amplifiers in the Individual Sensor Boards (ISBs) provided by Alphasense. Over the mixing ratio range of interest, the sensors' responses to the gases of interest are approximately linear. We derive mixing ratios from the observed voltages by subtracting an offset and then scaling by a constant (Eq. 4.1-4.4):

$$\text{CO}_\text{ambient} = (V_\text{CO} - \text{zero}_\text{CO})/k_\text{CO} \tag{4.1}$$

$$\text{NO}_\text{ambient} = (V_\text{NO} - \text{zero}_\text{NO})/k_\text{NO} \tag{4.2}$$

$$\text{NO}_{2\text{ambient}} = (V_{\text{NO}_2} - \text{zero}_{\text{NO}_2})/k_{\text{NO}_2} - (r_{\text{NO}-\text{NO}_2} \times \text{NO}_\text{ambient}) \tag{4.3a}$$
$$\text{NO}_{2\text{ambient}} = (V_{\text{NO}_2} - \text{zero}_{\text{NO}_2})/k_{\text{NO}_2} + (r_{\text{CO}_2-\text{NO}_2} \times \text{CO}_{2\text{ambient}}) \tag{4.3b}$$

$$\text{O}_{3\text{ambient}} = (V_{\text{O}_3} - \text{zero}_{\text{O}_3})/k_{\text{O}_3} - (r_{\text{NO}_2-\text{O}_3} \times \text{NO}_{2\text{ambient}}) \tag{4.4}$$

Here, CO, NO, NO$_2$, and O$_3$ with the subscript "ambient" refer to the gas mixing ratios (ppb) in air; V_{CO}, V_{NO}, V_{NO_2} and V_{O_3} are the signals (mV) measured by each sensor, which is

the voltage of the auxiliary electrode subtracted from the voltage of the working electrode; $zero_{CO}$, $zero_{NO}$, $zero_{NO_2}$, and $zero_{O_3}$ indicates the voltage measured in the absence of analyte; and k_{CO}, k_{NO}, k_{NO_2} and k_{O_3} represent the linear sensitivity factor that converts mV to ppb. Additional terms corresponding to the cross-sensitivities of the NO_2 and O_3 sensors appear in Eq. 4.3a, 4.3b, and 4.4, where r_{NO-NO_2} is the cross-sensitivity of the NO_2-B42F sensor to NO gas, $r_{CO_2-NO_2}$ is the cross-sensitivity of the NO_2-B43F sensor to CO_2 gas, and $r_{NO_2-O_3}$ is the cross-sensitivity of both the O_3-B421 and O_3-B431 sensors to NO_2 gas.

There are a total of 8 sensitivities and zero offsets, as well as 2 cross-sensitivity terms. All of these may also vary with time, temperature, and humidity. Thus we need a calibration strategy that constrains 10 parameters in a single instant as well as the variation of those 10 parameters in response to the environmental variables and time. We begin by characterizing the sensors in both laboratory and outdoor environments.

We evaluate BEACO$_2$N in terms of four factors: drift, noise, cross-sensitivity, and temperature dependence. The humidity dependence is included in the temperature dependence, as there is no evidence for independent humidity dependence and relative humidity exhibits an anti-correlation with temperature in the field. In the laboratory, a range of mixing ratios of target gases were delivered to a chamber containing the full suite of four Alphasense B4 sensors: CO, NO, NO_2, and O_3. Zero air was supplied by a Sabio 1001 Compressed Zero Air Source and blended with calibration gases using a ThermoScientific 146i Multi-Gas Calibrator.

Noise – Alphasense reports 2σ noise of ± 4, ± 1, ± 12, and ± 15 ppb for CO, NO, NO_2, and O_3, respectively over concentrations from 0 to 200 ppb at time resolution of a second. In our laboratory, noise ($\pm 2\sigma$) was measured for ambient ppb levels with 10 s time resolution and was seen to be ± 10ppb for CO, ± 3ppb for NO, ± 6ppb for NO_2 (NO_2-B42F and NO_2-B43F), and ± 12ppb for O_3 (O_3-B421 and O_3-B431).

Cross-Sensitivity – We measured the cross-sensitivity of all 4 of the trace gas sensors to the non-target gases. The NO_2 sensors and O_3 sensors were the only ones to exhibit sensitivity to other species. The O_3 sensor (O_3-B421 and O_3-B431) demonstrated 100% sensitivity to NO_2. This sensor is now being marketed by Alphasense as an odd oxygen ($O_x \equiv O_3 + NO_2$) sensor. In addition, the NO_2-B42F sensor was found to possess a significant NO sensitivity (130%) that exceeds the cross-sensitivity specified in the Alphasense documentation ($<$5%). The NO_2-B43F sensor was found to have 0.002% sensitivity to CO_2 gas, which is in the range of the cross-sensitivity specified in the Alphasense documentation ($<$0.1%). However, given that typical ambient CO_2 concentrations are four orders of magnitude larger than NO_2 concentrations, this relatively small cross-sensitivity to CO_2 gas manifests as a significant interference in the NO_2 sensors. These cross-sensitivities are represented in Eq. 4.3 and Eq. 4.4.
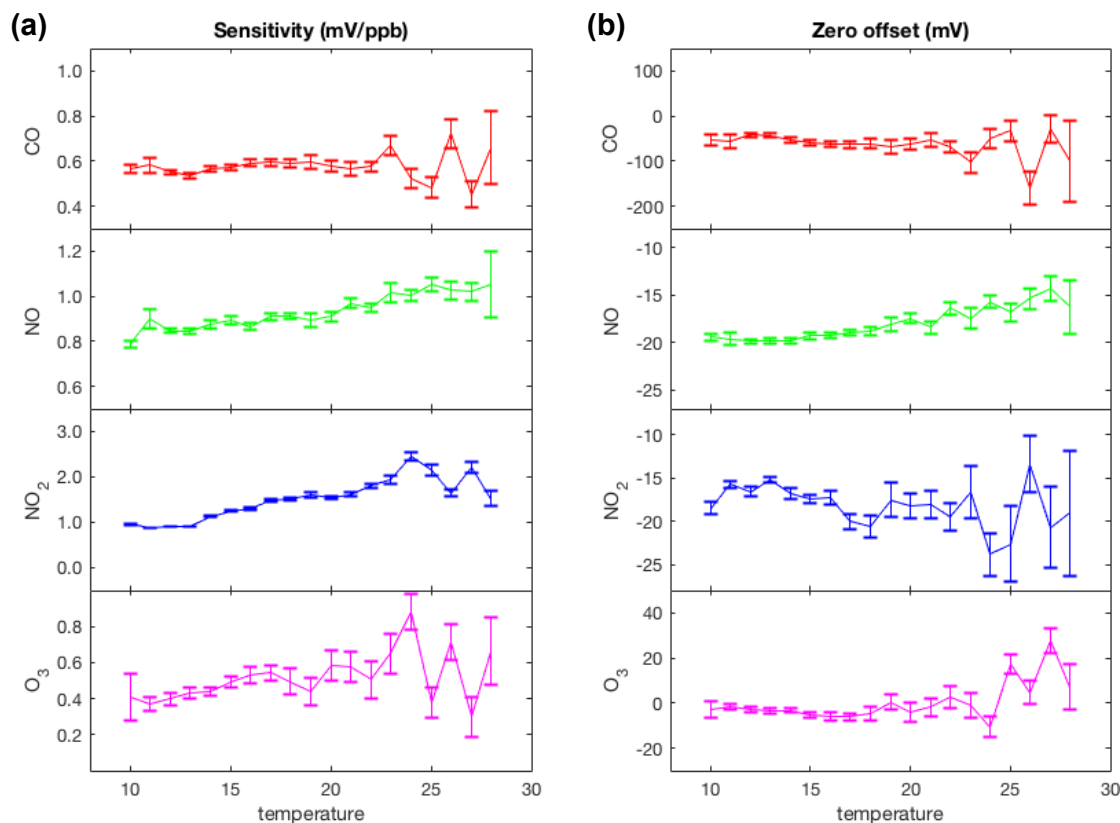
Figure 4.3: Representative temperature dependent sensitivities (a) and zero offsets (b) of the Alphasense electrochemical sensors calculated by comparing hourly averaged measurements from Laney College BEACO$_2$N node to measurements from a co-located reference instrument during February to April 2016.

Temperature Dependence – Electrochemical sensors are known to have temperature dependent sensitivities and zero offsets. Alphasense reports sensitivities and zero offsets for a temperature range between $-30°$C and 50°C. The sensitivities in their data sheets vary with temperature by $+0.1$ to $+0.3\% \, K^{-1}$ (referenced to sensitivity at 20°C) and the zero offsets are indicated to vary little except at high temperatures. We observed similar, but slightly larger variations via in situ comparison to co-located reference instruments. We observed temperature dependence in the sensitivities of $+0.3$ to $+5\% \, K^{-1}$ and no variation in the zero offset of the CO, NO$_2$, and O$_3$ sensors from 10°C to 24°C (Fig. 4.3). However, the zero offset of the NO sensor exhibited a strong temperature dependence of $0.34 \, mV \, K^{-1}$.

Drift – Two laboratory calibrations were performed roughly 10 weeks apart and the zero offsets and sensitivities are shown in Table 4.1. Over the 10-week interval, zero drift was equivalent to -15.9, -2.3, $+15.8$, and -12.7 ppb for CO, NO, NO$_2$, and O$_3$, respectively.

Table 4.1: Zero offsets and sensitivities of a representative quartet of Alphasense B4 electrochemical sensors derived via comparison to delivered reference gases during two separate laboratory calibration separated by an approximately 10-week interlude.

		May	August
O_3	Zero offset (mV)	-34.6417	-42.7629
	Sensitivity (mV ppb^{-1})	0.6404	0.2997
CO	Zero offset (mV)	108.9770	89.5812
	Sensitivity (mV ppb^{-1})	1.2192	1.0301
NO	Zero offset (mV)	-14.2030	-17.7801
	Sensitivity (mV ppb^{-1})	1.5758	1.2972
NO_2	Zero offset (mV)	-13.7159	-6.0649
	Sensitivity (mV ppb^{-1})	0.4842	0.3843

Alphasense reports the stability over time for the zero offset to be $< \pm 100$, 0 to 50, 0 to 20, and 0 to 20 ppb yr^{-1} for these sensors, respectively; over this 10 week interval, the observed zero drift was within the range of these specifications. However, it is a large fraction of the annual drift specification and further experiments would be warranted to test whether the zero measured is stable over a full year within the specified tolerances. The drift in the sensitivity (in % of k_x) was -15.9, -17.7, -20.6, and -53.2%. Alphasense reports <10, 0 to -20, -20 to -40, and < -20 to -40% yr^{-1} for CO, NO, NO$_2$, and O$_3$ calibration factors, respectively. We find that drift for the CO and O$_3$ sensitivities exceeded the manufacturer specifications, but that the NO and NO$_2$ sensitivity drifts were within the specified tolerances.

4.3   Model for Field Calibration

Here, we propose a model for field calibration that leverages (1) useful cross-sensitivities, (2) chemical conservation equations, (3) knowledge of the global and/or regional background of pollutants, and (4) assumptions based on well-known characteristics of urban air quality and local emissions. The result is a calibration procedure for the drift and temperature dependencies of the 10 calibration parameters that does not require co-location with a reference instrument or prior laboratory experiments for each sensor. The first constraint we apply is the O$_3$ sensors' cross-sensitivity to NO$_2$. Laboratory measurements indicate that this cross-sensitivity is 100% and we fix it at that value.

4.3.1 Regional ozone uniformity to calibrate the NO_2 and O_3 sensors' sensitivities

The NO, NO_2, and O_3 sensitivity can be derived from observations with higher quality instruments at nearby locations. Ozone is a secondary pollutant with small local scale variation, except in the very near field of NO emissions. The Bay Area Air Quality Management District (BAAQMD) maintains four TECO 49i ozone analyzers within the $BEACO_2N$ study area (see Fig. 4.1). We choose the closest site among these four regulatory monitoring sites to provide $O_{3ambient}$ as a constraint for multiple linear regression of Eq. 4.5 (derived from Eq. 4.2-4.4). Different $BEACO_2N$ nodes are thus referenced to different reference instruments.

$$O_{3\text{ambient}} = \frac{V_{O_3}}{k_{O_3}} - \frac{V_{NO_2}}{k_{NO_2}} + r_{NO-NO_2}\frac{V_{NO}}{k_{NO}} - \text{offset} \tag{4.5}$$

Here, offset is a combination of the zero offsets of the NO, NO_2, and O_3 sensors, all of which can be constrained as detailed in Sect. 3.2 below. The sensitivity of the O_3 and NO_2 sensors (k_{O_3} and k_{NO_2}), and relationship between the NO-NO_2 cross-sensitivity and the sensitivity of the NO sensor (r_{NO-NO_2}/k_{NO}) are obtained by multiple linear regression of Eq. 4.5.

4.3.2 Use of co-emitted gases in plumes to calibrate the CO and NO sensors' sensitivity

The CO and NO sensor cannot be constrained by cross sensitivity to the other gases. Instead, we constrain the sensitivity by insisting that the median emission factor of CO (or NO) per unit CO_2 corresponds to median values reported for the U.S. vehicle fleet. We express the emission factor (EF_X, ppb ppm^{-1}) of gas X, which is CO or NO, as in Eq. 4.6:

$$EF_X = \frac{\Delta X_{\text{ambient}}}{\Delta CO_{2\text{ambient}}} = \frac{1}{k_X}\frac{\Delta V_X}{\Delta CO_{2\text{ambient}}} \tag{4.6}$$

Our measurements of the concentration of CO_2 are described in Shusterman et al. (2016) and values for EF_{CO} and EF_{NO_x} are reported in Dallmann et al. (2013, see Table 4.2). We constrain the sensitivity of the CO and NO sensors in the network such that the median $\Delta X/\Delta CO_2$ of the plumes are equal to emission factors characteristic of the average vehicle fleet. The NO sensors' sensitivity is constrained by the emission factor of NO_x, estimating the upper limit of NO concentration.

Figure 4.4 shows an example of a measured plume and the derived $\Delta CO/\Delta CO_2$ ratio. We identify plumes as the local maximum found in a 10 min moving window, starting and ending at the local minima. Each plume is a few minutes in duration, representing an emission ratio averaged over several vehicles. Since diesel trucks have an order of magnitude higher NO_x emission factors compared to gasoline vehicles, the percentage of truck traffic near each site affects the median emission factors. The median freeway truck ratio varies little across the $BEACO_2N$ network, however, regions with a larger range of median truck ratios will have larger uncertainties or require a calibration approach that accounts for this variation.

Table 4.2: Reported emission factors of diesel and gasoline vehicles (Dallmann et al., 2011, 2012, 2013). Emissions from medium-duty and heavy-duty diesel trucks, which account for <1% of all vehicles, were removed to give the value for light-duty gasoline vehicles.

Vehicle type	CO emission factor $(\mathrm{g\,kg\,fuel^{-1}})$	NO_x emission factor $(\mathrm{g\,kg\,fuel^{-1}})$
Heavy-duty diesel trucks	8.0 ± 1.2	28.0 ± 1.5
Light-duty gasoline vehicles	14.3 ± 0.7	1.90 ± 0.08
99% gasoline vehicles, 1% diesel trucks	14.2 ± 0.7	2.29 ± 0.12
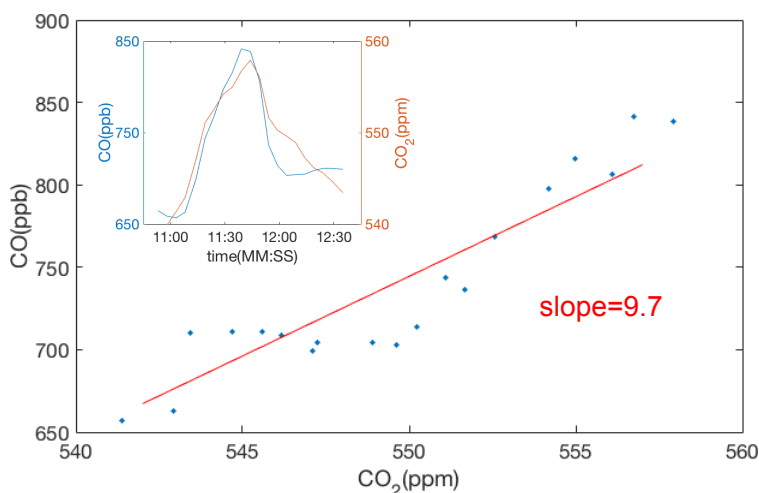
Figure 4.4: Example of CO plume identification and regression against CO_2 to find the CO emission factor using raw, 10 s data. The derived CO emission ratio (CO/CO_2) for this example is $9.7\,\mathrm{ppb\,ppm^{-1}}$.

4.3.3 Use of chemical conservation equations near emissions to calibrate the NO, NO_2 and O_3 sensors' zero offsets

We are able to constrain the zero offsets of NO, NO_2 and O_3 sensors by taking advantage of proximity to local emission sources and the following chemical conservation equations.

$$NO + O_3 \rightarrow NO_2 + O_2 \tag{R1}$$

$$NO_2 + h\nu \rightarrow NO + O \tag{R2}$$

$$O + O_2 + M \rightarrow O_3 + M \tag{R3}$$

These three reactions result in a steady-state relationship among the nitrogen oxides ($O_x \equiv O_3 + NO_2$) and ozone. At nighttime, reaction (R2) does not occur due to the absence of sunlight. In the absence of emissions, the NO concentration goes to zero on nights with
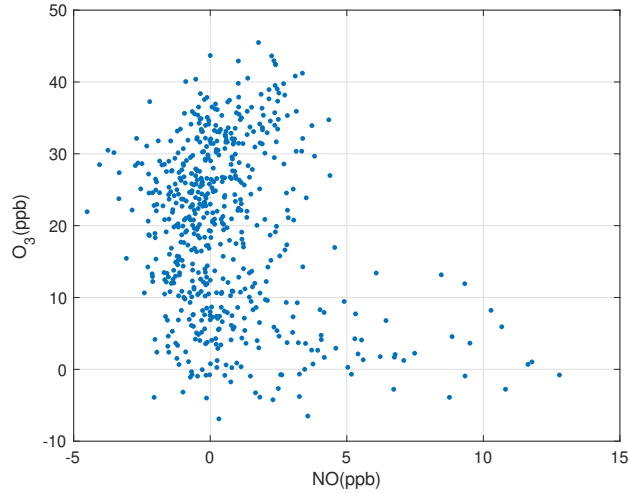
Figure 4.5: Representative month of 1 min averaged NO and O_3 measurements taken between 00:00 and 03:00; plumes excluded.

sufficient O_3. Conversely, near strong emission sources, NO is found in excess of ozone and the O_3 concentration goes to zero (see Fig. 4.5). Using this logic, we identify times between 00:00 to 03:00 when there is zero NO or O_3 to define the zero offsets of the NO and O_3 sensors, using 1 min averaged data with plumes excluded (see Sect. 4.3.2 for details of the plume identification procedure).

The NO_2 offset can be determined using the pseudo-steady state (PSS) approximation. We estimate the NO_2 concentration through Eq. 4.7:

$$j_{NO_2} [NO_2] = k_{NO\text{-}O_3} [NO] [O_3] \tag{4.7}$$

Here, j_{NO_2} (in units of s^{-1}) is the photolysis rate constant for reaction (R2) and $k_{NO\text{-}O_3}$ (in units of cm^3 molecule^{-1} s^{-1}) is the rate constant for reaction R1. $[X]$ expresses the concentration of gas X in units of molecules cm^{-3}. We use sensitivity corrected (see Section 4.3.1 and 4.3.2), 1 min average NO and O_3 concentrations measured from 12:00 to 15:00, and select data with a time derivative of O_3 near zero to insure that the measurements reflect air that has achieved steady state. The NO_2 concentration at PSS is derived using Eq. 4.7 and the NO_2 offset is chosen to insure the calculated and observed NO_2 are equal. NO_2 is also produced through the reaction of HO_2/RO_2 with NO, but this is omitted from the right hand side of Eq. 4.7, resulting in a lower bound of the true NO_2 concentration. Estimated NO_2 is therefore low by about 5 % in winter and as much as 30 % in summer. If higher accuracy is needed, the reaction of HO_2/RO_2 with NO could be considered to reduce this bias.

4.3.4 Use of global background to calibrate the CO sensors' zero offset

To infer the zero offset of the CO sensor, we follow the procedure outlined in Shusterman et al. (2016) for CO_2 sensors. We assume the signal measured at a given site is decomposed as in Eq. 4.8:

$$[CO]_{ambient} = [CO]_{background} + [CO]_{local} + offset \tag{4.8}$$

The measurement of the pollutant CO ($[CO]_{ambient}$) is the sum of regional and local signals ($[CO]_{background}$ and $[CO]_{local}$, respectively), as well as some offset from the true concentration (offset). Assuming the monthly minimum concentration measured at a given site represents $[CO]_{background}$, this background signal is compared to that measured at a "supersite" of reference instruments located within the network domain, allowing the offset to be derived. We also assume that when $[CO]_{ambient}$, as well as $[CO]_{local}$, is minimum in each day, the concentration measured at a given site has a constant deviation from the background signal. This is a reasonable assumption for the BEACO$_2$N domain as the dominant wind pattern frequently brings unpolluted air from the Pacific Ocean.

4.3.5 Temperature dependence and temporal drift

In order to account for the temperature and time dependence of calibration parameters, we apply the calibration process described in Sect. 4.3.1 through 4.3.4 for temperature increments of 1°C within a 3-month running window. Then, we are able to define a temperature dependent sensitivity and zero offset, which is used to convert the measured voltages to mixing ratios. In this way, we can also evaluate temporal drift with monthly resolution. The calibration procedure can be repeated for shorter time intervals if wider temperature windows are used.

4.4 Evaluation with reference observation

We evaluate the efficacy of our calibration method using a BEACO$_2$N node co-located with reference instruments at the Laney College monitoring site maintained by the Bay Area Air Quality Management District (BAAQMD). Here we consider data collected from February to April 2016, calibrate it according to the procedure described above (following Sect. 4.3.1 to 4.3.5), and compare it against the BAAQMD data. Reference data is collected by a TECO 48i CO analyzer and a TECO 42i NO_x analyzer. Ozone data from the "Oakland West" location, the closest ozone-monitoring site maintained by BAAQMD, was used for multiple linear regression of Eq. 4.5. The zero offset for CO was calculated using BAAQMD data from the Bodega Bay background site (see Fig. 4.1; Guha et al., 2016) as local "supersite" data was unavailable during this period. A background site closer to the network would likely improve our ability to constrain the CO zero offset; a reference instrument for that purpose was installed in summer 2017.

Table 4.3: Mean absolute error of comparison between regional O_3 and hourly averaged BEACO$_2$N O_3 measurements derived from multiple linear regression models of increasing complexity between February and April 2016.

Regression Models		Mean absolute error (ppb)
$O_{3\text{true}} = \frac{V_{O_3}}{k_{O_3}} - \text{offset}$	Linearity of observed voltages and gas concentration	14.4063
$O_{3\text{true}} = \frac{V_{O_3}}{k_{O_3}} - \frac{V_{NO_2}}{k_{NO_2}} - \text{offset}$	O_3 sensor's cross-sensitivity correction	10.6795
$O_{3\text{true}} = \frac{V_{O_3}}{k_{O_3}} - \frac{V_{NO_2}}{k_{NO_2}} + r_{NO-NO_2}\frac{V_{NO}}{k_{NO}} - \text{offset}$	NO_2 and O_3 sensor's cross-sensitivity correction	8.8172
$O_{3\text{true}} = \frac{V_{O_3}}{k_{O_3}} - \frac{V_{NO_2}}{k_{NO_2}} + r_{NO-NO_2}\frac{V_{NO}}{k_{NO}} - \text{offset}$	Adding temperature correction	8.1360

In our calibration procedure, the cross-sensitivities and temperature dependence are corrected for better accuracy. Table 4.3 shows the reduction in mean absolute error (MAE) that results when cross-sensitivity and temperature dependence issues are considered during multiple linear regression of Eq. 4.5. Here, MAE is calculated after conducting the sensitivity correction explained in Section 4.3.1, but before the offset correction in Section 4.3.3. Fully calibrated, hourly averaged BEACO$_2$N sensor data is compared to reference data in Fig. 4.6. For NO, NO_2, O_3, and CO the mixing ratio measured agrees reasonably well with the reference instrument with correlation coefficients of 0.88, 0.61, 0.69, and 0.74 and MAE of 3.63, 4.12, 5.04, and 54.93 ppb, respectively. The noise ($\pm 2\sigma$) in the differences between the calibrated hourly BEACO$_2$N data and reference data is 9.74 ppb for NO, 9.97 ppb for NO_2, 13.04 ppb for O_3, and 116.23 ppb for CO. These noise values are dominated by the Alphasense noise except in the case of CO, where noise is evenly split between the low-cost electrochemical sensors and the reference instruments.

4.5 Examples of Source Attribution using emission ratios

Figure 4.7 shows a week-long time series of fully calibrated air quality data from four BEACO$_2$N sites in 2017 (see Fig. 4.1). BEACO$_2$N nodes capture the short-term variability associated with local emissions, superimposed on the diurnal variation caused by mixing and changes in the height of the boundary layer. Large mixing ratios of NO, NO_2, and O_3 are observed at the Hercules and Ohlone sites, likely representing strong NO_x emissions from an oil refinery nearby. The spatial variability of trace gases observed at these 4 BEACO$_2$N sites provides a more diverse perspective on emissions compared to that provided by the one
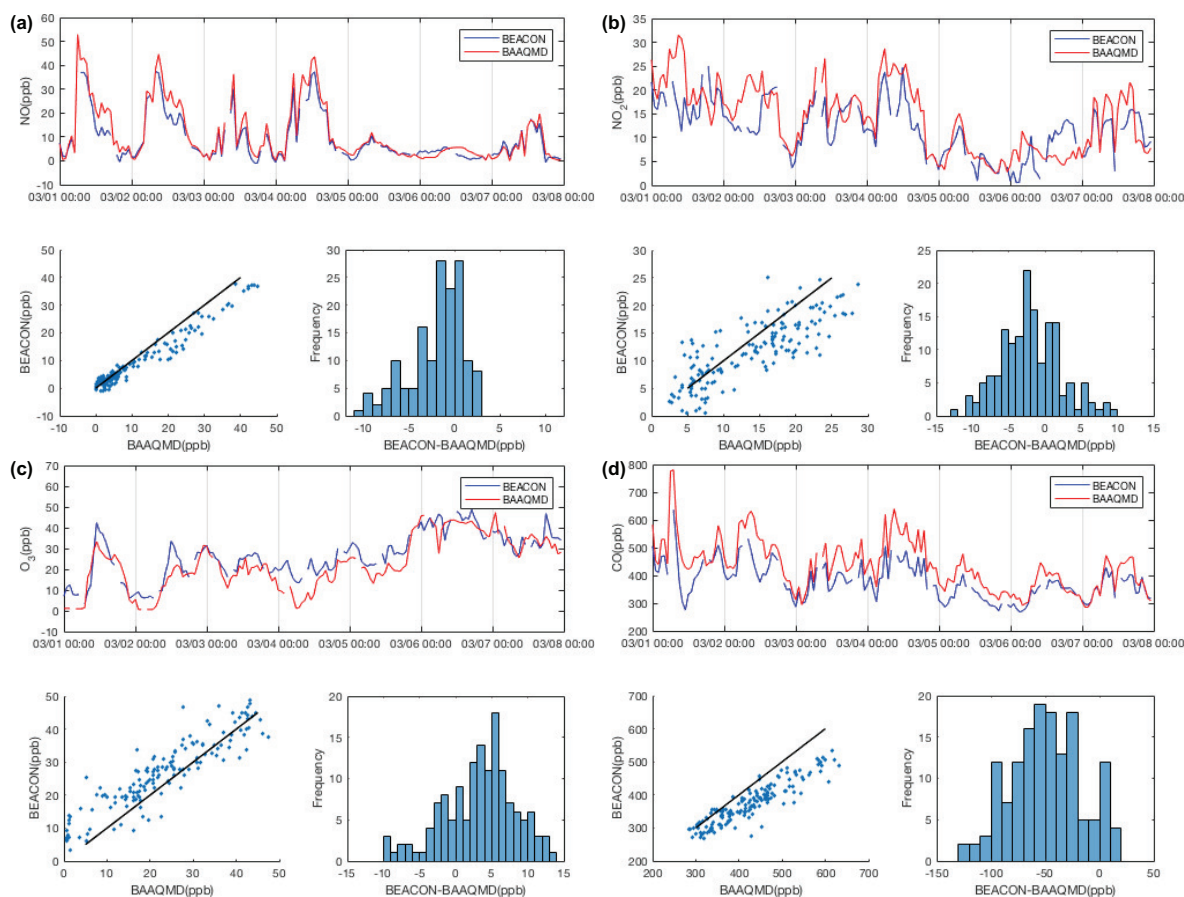
Figure 4.6: Time series (top), direct comparison (bottom left), and histogram (bottom right) of hourly averaged (a) NO, (b) NO_2, (c) O_3, (d) CO mixing ratios from a representative week of calibrated BEACO$_2$N and BAAQMD reference data. Black line in left plot on the left indicates the 1:1 line.

regulatory monitoring site in the vicinity.

The most widely used emission ratios, CO/CO_2 ratio, was investigated to show the feasibility of using the relationship between trace gases. Figure 4.8 shows the emission ratios of CO and CO_2 observed from a BEACO$_2$N node located 220 m away from the highway (LCC; see Fig. 4.9). The slope that represents CO/CO_2 ratio varies from 4.0 to 7.5 ppb/ppm depending on the time of day. The ratio is lower at early morning closer to the reported CO/CO_2 ratio of diesel trucks, and higher at late evening closer to the reported CO/CO_2 ratio of gasoline cars. From this we can infer that the ratio of trucks on the highway is higher at early morning compared to late evening. Indeed, the diel cycle of truck ratio reflects the same pattern.
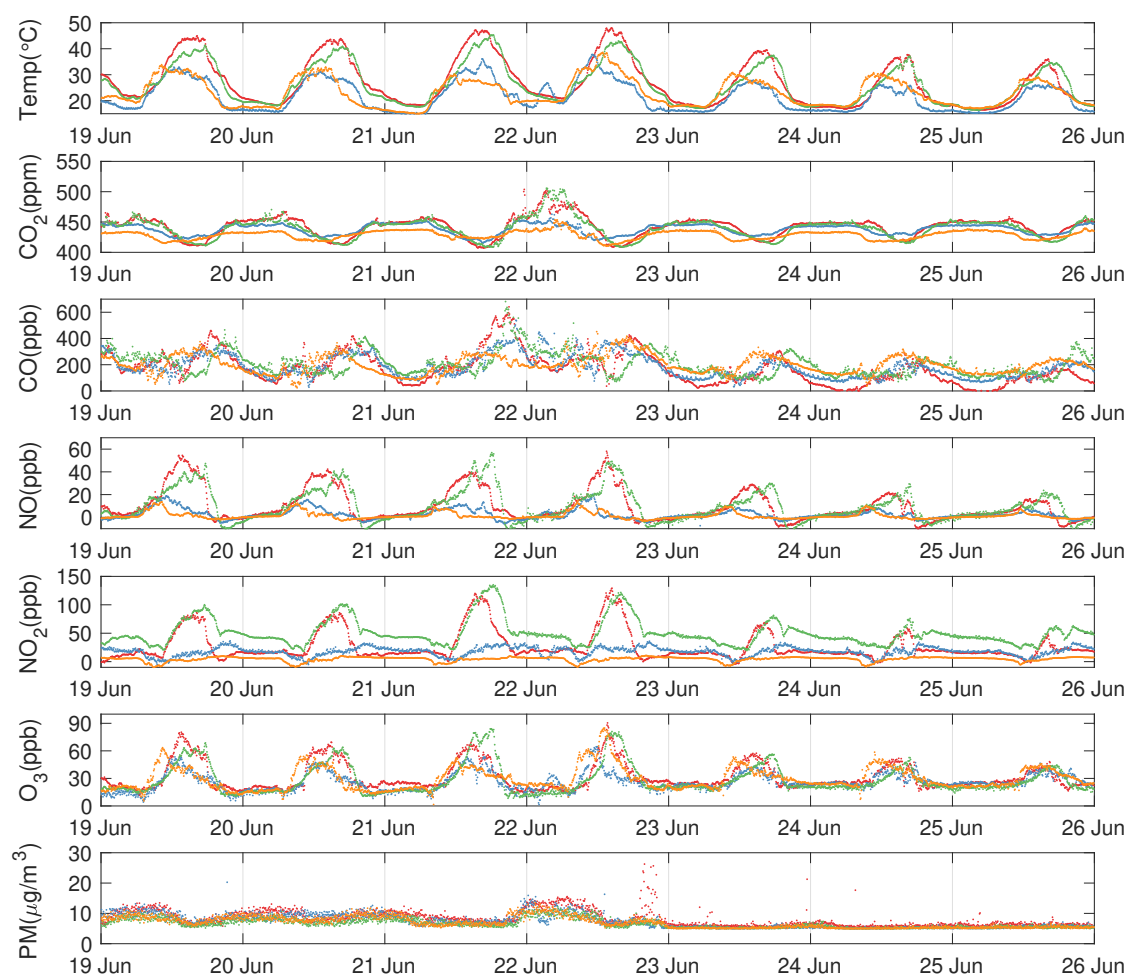
Figure 4.7: Time series of fully calibrated 5 min averaged BEACO₂N data from a representative week at 4 sites deployed in 2017. Observations from the Hercules, Ohlone, Washington, and Madera sites are plotted in red, green, orange, and blue, respectively. Particulate matter is converted to units of mass concentration according to Holstius et al. (2014).
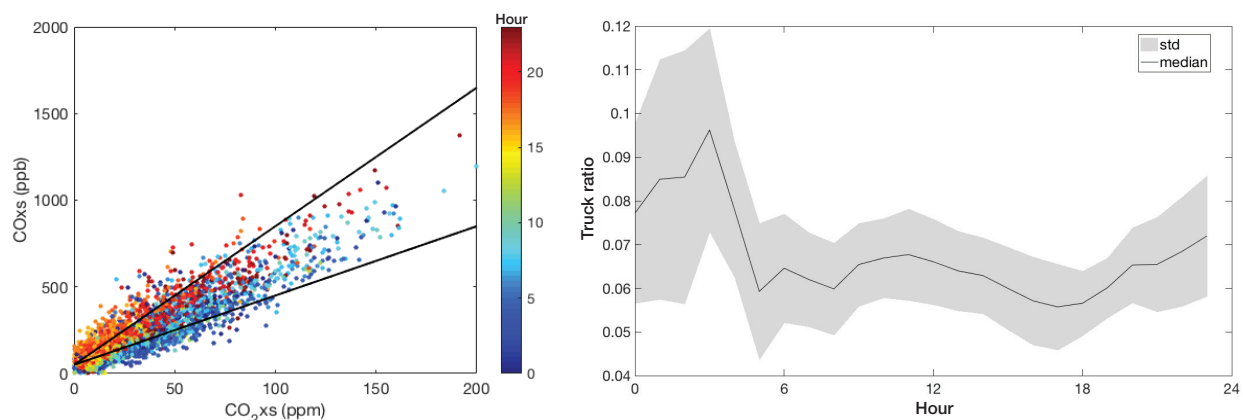
Figure 4.8: Relationship between observed CO_{XS} and CO_{2XS} (left) and median diel cycle of observed truck ratio (right; http://pems.dot.ca.gov/) at LCC. CO_{XS} and CO_{2XS} are background concentrations subtracted from CO and CO_2. Black lines on the left plot indicate reported CO/CO_2 ratio of diesel trucks (bottom) and gasoline cars (top).

Figure 4.9 demonstrates the emission ratios of CO and CO_2 observed from 5 different BEACO$_2$N sites in September and October 2017. Most of the measurements fits between the two lines representing reported CO/CO_2 ratio of diesel trucks and gasoline cars (see Table 4.2). This reveals that the majority of local emission sources are transportation at all 5 sites. However, 2 sites in Contra Costa county (COL and PER) and 1 site in San Francisco county (EXE) show observations with high CO/CO_2 ratio. The period when this high CO/CO_2 ratio was measured overlap with the dates that (1) smoke from the Nevada and Butte county wildfires, and northern California and Oregon wildfires moving into the Bay Area was reported (from August 31, 2017 to September 4, 2017), and (2) the Napa and Sonoma county wildfires was ongoing (from October 8, 2017 to October 31, 2017). The use of CO/CO_2 ratio together with a high-density monitoring network provides the spatial pattern of areas affected by wildfire emissions. Smokes from the wildfires came down following the coast, not affecting more inland regions.

4.6 Conclusions

We have described the characteristics and implementation of the low-cost trace gas sensors for a high-density monitoring network. We demonstrate a low-cost, in-field calibration method that allows continuous measurements and quantitative analysis of it. The Alphasense B4 electrochemical gas sensors are able to detect typical diurnal cycles in gas concentrations as well as short-term changes corresponding to chemical reactions and local emissions. The calibrated dataset demonstrates the pattern of specific emissions over time and space using
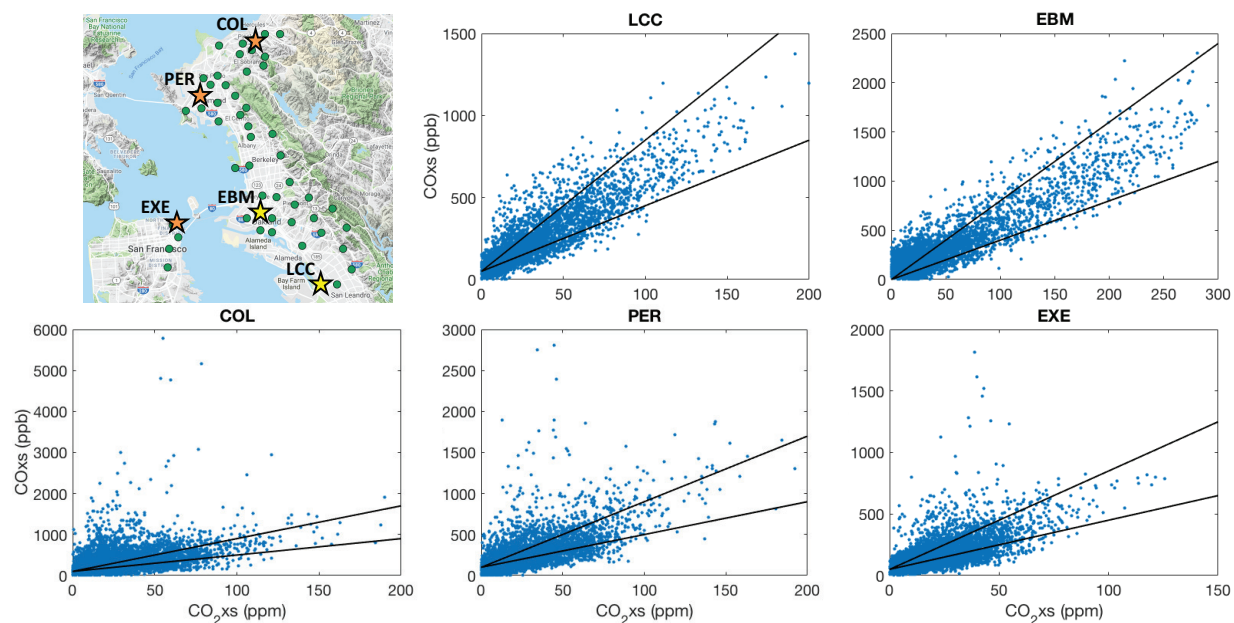
Figure 4.9: Map of 5 representative BEACO2N sites (top left) and relationship between observed CO_{XS} and CO_{2XS} at each site. CO_{XS} and CO_{2XS} are background concentrations subtracted from CO and CO_2. Black lines in each plot indicate reported CO/CO_2 ratio of diesel trucks (bottom) and gasoline cars (top).

the relationship between co-emitted trace gases. Through this work, we can realize the promise of low-cost, high-density sensor networks associated with the emission ratio method as a viable approach to monitor individual emission sectors. Future work is needed to construct quantitative interpretation of emission patterns from the observations.

Chapter 5

Conclusions

In order to reduce greenhouse gas emissions in cities, accurate knowledge of each city's greenhouse gas emission budget, including the location and sectoral contributions of each source, is required. High-density monitoring networks provide a powerful tool to attribute emissions to specific source sectors as they preserve signals from local sources.

In this dissertation, I have developed methodologies to constrain emissions from specific sectors using a low-cost, high-density sensor network: the Berkeley Environmental Air-quality & CO_2 Observation Network (BEACO$_2$N). In Chapter 2, I demonstrated a novel approach to using dense network observations combined with Gaussian plume models to estimate the average emission rate per vehicle instead of the city-wide total emissions. Multiple sites are collectively analyzed to achieve reduced uncertainty from Shusterman et al. (2018). I demonstrate a path to achieving the accuracy needed to detect interannual variability in mobile emissions. For example, better understanding of the mixing dynamics and a more explicit approach to account for the variation in urban CO_2 will improve the method.

In Chapter 3, I extended this model to evaluate biogenic emission and uptake of CO_2 which is unique in its capability to identify biogenic fluxes without using a land-use or other biospheric model. This method produces regional scale fluxes from the ambient CO_2 measurements that correspondence to seasonal variation of CO_2 uptake measured from space. The ability to derive biogenic CO_2 emissions and uptake on a fine spatial and temporal scale using a high-density sensor network will enhance our understanding of processes affecting urban biogenic fluxes.

In Chapter 4, I demonstrate the feasibility of utilizing the relationships between trace gases that are co-emitted from combustion to characterize the relative fluxes from various emission sources. I describe a unique approach to calibration of electrochemical sensors in a newly developed observing tool, the BEACO$_2$N high-density sensor network, that does not require laboratory experiments or co-location with a reference instrument. Sensors are calibration

in field taking advantage of the prior knowledge about urban air quality and local emissions. Calibrated trace gas measurements can be used to quantify source specific emissions with reduces uncertainty.

In this thesis, I describe significant progress on assessment of urban greenhouse gas emissions from mobile and biogenic emissions using the BEACO$_2$N high-density sensor network. One important area of future research are emissions from industrial point sources, which are one of the 3 major sources in San Francisco Bay Area. It is expected that the comprehensive spatial coverage of the BEACO$_2$N network will capture the narrow plumes evolving from the point source enabling quantification of their emissions. Another direction for future research should be to take advantage of the additional measurements (CO, NO, NO$_2$, O$_3$, and particulate matter) collected by BEACO$_2$N. These additional tracers offer the opportunity for source attribution and quantification of the relative contribution even without the use of activity data. It can also provide additional constraints on emissions estimated from the Gaussian plume model to achieve even greater accuracy.

These ideas focus on a single city. A second research theme for future work should be an inter-city comparison. Additional BEACO$_2$N sites have already been established in secondary locations in Houston and New York City. Los Angeles and Scotland are the intended next locations with deployments expected in early 2021. Understanding the similarities and differences across the cities using a common observation system will be an exciting advance. For example, Houston has a shipping port and a large chemical industry to the southeast and the urban population resides predominantly to the west and north. Much of the region is low-rise buildings. In contrast, the density of skyscrapers in New York City creates large street canyon effects and locations for sensor deployments to assess emissions are likely affected by the associated complex circulations and transport dynamics.

Finally, future work should leverage atmospheric transport models together with long-term BEACO$_2$N observations at high temporal and spatial resolution to resolve the highly variable spatiotemporal patterns of the greenhouse gas emissions. An atmospheric modeling framework used with multi-species inversion will attribute the sources with high fidelity, and the framework used with an urban scale CO$_2$ inventory will further provide insights on physical processes governing urban CO$_2$.

Bibliography

Bart, M., D. E. Williams, B. Ainslie, I. Mckendry, J. Salmond, S. K. Grange, M. Alavi-shoshtari, D. Steyn and G. S. Henshaw. *High density ozone monitoring using gas sensitive semi-conductor sensors in the lower fraser valley, british columbia*. Environmental Science and Technology, volume 48; pages 3970–3977, 2014.

Bay Area Air Quality Management District. *2017 clean air plan: Spare the air, cool the climate*, 2017.

Bishop, G. A., B. G. Schuchmann and D. H. Stedman. *Heavy-duty truck emissions in the south coast air basin of california*. Environmental science & technology, volume 47, no. 16; pages 9523–9529, 2013.

Borrego, C., A. M. Costa, J. Ginja, M. Amorim, M. Coutinho, K. Karatzas, T. Sioumis, N. Katsifarakis, K. Konstantinidis, S. De Vito, E. Esposito, P. Smith, N. André, P. Gérard, L. A. Francis, N. Castell, P. Schneider, M. Viana, M. C. Minguillón, W. Reimringer, R. P. Otjes, O. von Sicard, R. Pohle, B. Elen, D. Suriano, V. Pfister, M. Prato, S. Dipinto and M. Penza. *Assessment of air quality microsensors versus reference methods: The eunetair joint exercise*. Atmospheric Environment, volume 147, no. 2; pages 246–263, 2016. ISSN 18732844. doi:10.1016/j.atmosenv.2016.09.050.

Bovensmann, H., M. Buchwitz, J. P. Burrows, M. Reuter, T. Krings, K. Gerilowski, O. Schneising, J. Heymann, A. Tretner and J. Erzinger. *A remote sensing technique for global monitoring of power plant co2 emissions from space and related applications*. Atmospheric Measurement Techniques, volume 3, no. 4; pages 781–811, 2010. ISSN 18671381. doi:10.5194/amt-3-781-2010.

Bréon, F., G. Broquet, V. Puygrenier, F. Chevallier, I. Xueref-Remy, M. Ramonet, E. Dieudonné, M. Lopez, M. Schmidt, O. Perrussel et al. *An attempt at estimating paris area co 2 emissions from atmospheric concentration measurements*. Atmospheric Chemistry & Physics, volume 15, no. 4, 2015.

California Air Resources Board. *The 2017 climate change scoping plan update: The proposed strategy for achieving california's 2030 greenhouse gas target*, 2017a.

California Air Resources Board. *California greenhouse gas emissions for 2000 to 2017: Trends of emissions and other indicators*, 2017b.

Change, I. C. et al. *Mitigation of climate change.* Contribution of Working Group III to the Fifth Assessment Report of the Intergovernmental Panel on Climate Change, volume 1454, 2014.

Chevallier, F., F. M. Bréon and P. J. Rayner. *Contribution of the orbiting carbon observatory to the estimation of co2 sources and sinks: Theoretical study in a variational data assimilation framework.* Journal of Geophysical Research Atmospheres, 2007. ISSN 01480227. doi:10.1029/2006JD007375.

Choi, W., A. Winer and S. Paulson. *Factors controlling pollutant plume length downwind of major roadways in nocturnal surface inversions.* Atmos. Chem. Phys, volume 14; pages 6925–6940, 2014.

Cox, R. M. *The use of passive sampling to monitor forest exposure to o 3 , no 2 and so 2 : a review and some case studies .* Environmental Pollution, volume 126, no. 2; pages 301–311, 2003. doi:10.1016/S0269-7491(03)00243-4.

Crisp, D. *Nasa orbiting carbon observatory: measuring the column averaged carbon dioxide mole fraction from space.* Journal of Applied Remote Sensing, 2008. ISSN 1931-3195. doi:10.1117/1.2898457.

Dallmann, T. R., S. J. DeMartini, T. W. Kirchstetter, S. C. Herndon, T. B. Onasch, E. C. Wood and R. A. Harley. *On-road measurement of gas and particle phase pollutant emission factors for individual heavy-duty diesel trucks.* Environmental science & technology, volume 46, no. 15; pages 8511–8518, 2012.

Dallmann, T. R., R. A. Harley and T. W. Kirchstetter. *Effects of diesel particle filter retrofits and accelerated fleet turnover on drayage truck emissions at the port of oakland.* Environmental science & technology, volume 45, no. 24; pages 10 773–10 779, 2011.

Dallmann, T. R., T. W. Kirchstetter, S. J. DeMartini and R. A. Harley. *Quantifying on-road emissions from gasoline-powered motor vehicles: Accounting for the presence of medium- and heavy-duty diesel trucks.* Environmental science & technology, volume 47, no. 23; pages 13 873–13 881, 2013.

Dee, D. P., S. M. Uppala, A. J. Simmons, P. Berrisford, P. Poli, S. Kobayashi, U. Andrae, M. A. Balmaseda, G. Balsamo, P. Bauer, P. Bechtold, A. C. Beljaars, L. van de Berg, J. Bidlot, N. Bormann, C. Delsol, R. Dragani, M. Fuentes, A. J. Geer, L. Haimberger, S. B. Healy, H. Hersbach, V. E. Hólm, L. Isaksen, P. Kållberg, M. Köhler, M. Matricardi, A. P. Mcnally, B. M. Monge-Sanz, J. J. Morcrette, B. K. Park, C. Peubey, P. de Rosnay, C. Tavolato, J. N. Thépaut and F. Vitart. *The era-interim reanalysis: Configuration and performance of the data assimilation system.* Quarterly Journal of the Royal Meteorological Society, volume 137, no. 656; pages 553–597, 2011. ISSN 00359009. doi:10.1002/qj.828.

Djuricin, S., D. E. Pataki and X. Xu. *A comparison of tracer methods for quantifying co2 sources in an urban region.* Journal of Geophysical Research, volume 115, no. 14; pages 1–13, 2010. doi:10.1029/2009JD012236.

Eldering, A., T. E. Taylor, C. W. O'Dell and R. Pavlick. *The oco-3 mission: Measurement objectives and expected performance based on 1 year of simulated data.* Atmospheric Measurement Techniques, 2019. ISSN 18678548. doi:10.5194/amt-12-2341-2019.

Gately, C. K. and L. R. Hutyra. *Large uncertainties in urban-scale carbon emissions.* Journal of Geophysical Research: Atmospheres, volume 122, no. 20; pages 11,242–11,260, 2017. ISSN 21698996. doi:10.1002/2017JD027359.

Guha, A., J. Bower, P. Martien and I. Perkins. *Timeseries of atmospheric dry air mole fractions from continuous measurements at fixed-site ghg monitoring stations in the san francisco bay area, california*, 2016.

Gurney, K. R., J. Liang, R. Patarasuk, Y. Song, J. Huang and G. Roest. *The vulcan version 3.0 high-resolution fossil fuel co2 emissions for the united states.* Journal of Geophysical Research: Atmospheres, 2020. ISSN 2169-897X. doi:10.1029/2020jd032974.

Gurney, K. R., R. Patarasuk, J. Liang, Y. Song, D. Oamp;apos;Keeffe, P. Rao, J. R. Whetstone, R. M. Duren, A. Eldering and C. E. Miller. *The hestia fossil fuel co2 emissions data product for the los angeles megacity (hestia-la).* Earth System Science Data, volume 11; pages 1309–1335, 2019. doi:10.5194/essd-2018-162.

Gurney, K. R., I. Razlivanov, Y. Song, Y. Zhou, B. Benes and M. Abdul-Massih. *Quantification of fossil fuel co2 emissions on the building/street scale for a large u.s. city.* Environmental Science and Technology, 2012.

Hagan, D. H., G. Isaacman-VanWertz, J. P. Franklin, L. M. M. Wallace, B. D. Kocar, C. L. Heald and J. H. Kroll. *Calibration and assessment of electrochemical air quality sensors by co-location with regulatory-grade instruments.* Atmospheric Measurement Techniques, volume 11, no. 1; pages 315–328, January 2018. doi:10.5194/amt-11-315-2018.

Haugen, M. J., G. A. Bishop, A. Thiruvengadam and D. K. Carder. *Evaluation of heavy- and medium-duty on-road vehicle emissions in california's south coast air basin.* Environmental Science and Technology, volume 52, no. 22; pages 13 298–13 305, 2018. ISSN 15205851. doi:10.1021/acs.est.8b03994.

Hedelius, J. K., S. Feng, C. M. Roehl, D. Wunch, P. W. Hillyard, J. R. Podolske, L. T. Iraci, R. Patarasuk, P. Rao, D. O'Keeffe, K. R. Gurney, T. Lauvaux and P. O. Wennberg. *Emissions and topographic effects on column co2 (xco2) variations, with a focus on the southern california megacity.* Journal of Geophysical Research, volume 122, no. 13; pages 7200–7215, 2017. ISSN 21562202. doi:10.1002/2017JD026455.

Hedelius, J. K., J. Liu, T. Oda, S. Maksyutov, C. M. Roehl, L. T. Iraci, J. R. Podolske, P. W. Hillyard, J. Liang, K. R. Gurney, D. Wunch and P. O. Wennberg. *Southern california megacity co2, ch4, and co flux estimates using ground-and space-based remote sensing and a lagrangian model.* Atmospheric Chemistry and Physics, volume 18, no. 22; pages 16 271–16 291, 2018. ISSN 16807324. doi:10.5194/acp-18-16271-2018.

Hedelius, J. K., C. Viatte, D. Wunch, C. M. Roehl, G. C. Toon, J. Chen, T. Jones, S. C. Wofsy, J. E. Franklin, H. Parker, M. K. Dubey and P. O. Wennberg. *Assessment of errors and biases in retrievals of xco2 , xch4 , xco , and xn2o from a 0.5 cm 1 resolution solar-viewing spectrometer.* Atmospheric Measurement Techniques, volume 2; pages 3527–3546, 2016. doi:10.5194/amt-9-3527-2016.

Holstius, D. M., A. Pillarisetti, K. R. Smith and E. Seto. *Field calibrations of a low-cost aerosol sensor at a regulatory monitoring site in california.* Atmospheric Measurement Techniques, volume 7, no. 4; pages 1121–1131, April 2014. doi:10.5194/amt-7-1121-2014.

Jerrett, M., D. Donaire-gonzalez, O. Popoola, R. Jones, R. C. Cohen, E. Almanza, D. A. Nazelle, I. Mead, G. Carrasco-turigas, T. Cole-hunter, M. Triguero-mas, E. Seto and M. Nieuwenhuijsen. *Validating novel air pollution sensors to improve exposure estimates for epidemiological analyses and citizen science.* Environmental Research, volume 158, no. April; pages 286–294, 2017. ISSN 0013-9351. doi:10.1016/j.envres.2017.04.023.

Jiao, W., G. Hagler, R. Williams, R. Sharpe and R. Brown. *Community air sensor network (cairsense) project : Evaluation of low-cost sensor performance in a suburban environment in the southeastern united states.* Atmospheric Measurement Techniques, volume 9; pages 5281–5292, 2016. doi:10.5194/amt-9-5281-2016.

Kim, J., A. A. Shusterman, K. J. Lieschke, C. Newman and R. C. Cohen. *The berkeley atmospheric co2 observation network: Field calibration and evaluation of low-cost air quality sensors.* Atmospheric Measurement Techniques, volume 11, no. 4; pages 1937–1946, 2018. ISSN 18678548. doi:10.5194/amt-11-1937-2018.

Kort, E. A., W. M. Angevine, R. Duren and C. E. Miller. *Surface observations for monitoring urban fossil fuel co2 emissions : Minimum site location requirements for the los angeles megacity.* Journal of Geophysical Research, volume 118; pages 1–8, 2013. doi: 10.1002/jgrd.50135.

Kort, E. A., C. Frankenberg, C. E. Miller and T. Oda. *Space-based observations of megacity carbon dioxide.* Geophysical Research Letters, volume 39, no. 17; pages 1–5, 2012. ISSN 00948276. doi:10.1029/2012GL052738.

Krupa, S. and A. Legge. *Passive sampling of ambient, gaseous air pollutants: an assessment from an ecological perspective.* Environmental Pollution, volume 107, no. 1; pages 31–45, January 2000. doi:10.1016/s0269-7491(99)00154-2.

Kuze, A., H. Suto, M. Nakajima and T. Hamazaki. *Thermal and near infrared sensor for carbon observation fourier-transform spectrometer on the greenhouse gases observing satellite for greenhouse gases monitoring.* Applied Optics, 2009. ISSN 15394522. doi:10.1364/AO.48.006716.

Lauvaux, T., K. R. Gurney, N. L. Miles, K. J. Davis, S. J. Richardson, A. Deng, B. J. Nathan, T. Oda, J. A. Wang, L. Hutyra and J. C. Turnbull. *Policy-relevant assessment of urban co2emissions.* Environmental Science and Technology, volume 54, no. 16; pages 10 237–10 245, 2020. ISSN 15205851. doi:10.1021/acs.est.0c00343.

Lauvaux, T., N. L. Miles, A. Deng, S. J. Richardson, M. O. Cambaliza, K. J. Davis, B. Gaudet, K. R. Gurney, J. Huang, D. O'Keefe, Y. Song, A. Karion, T. Oda, R. Patara-suk, I. Razlivanov, D. Sarmiento, P. Shepson, C. Sweeney, J. C. Turnbull and K. Wu. *High-resolution atmospheric inversion of urban co2 emissions during the dormant season of the indianapolis flux experiment (influx).* Journal of Geophysical Research, volume 121, no. 10; pages 5213–5236, 2016. ISSN 21562202. doi:10.1002/2015JD024473.

Liu, J., K. W. Bowman, M. Lee, D. K. Henze, N. Bousserez, H. Brix, G. J. Collatz, D. Men-emenlis, L. Ott, S. Pawson, D. Jones and R. Nassar. *Carbon monitoring system flux estimation and attribution: Impact of acos-gosat xco2 sampling on the inference of terres-trial biospheric sources and sinks.* Tellus, Series B: Chemical and Physical Meteorology, 2014. ISSN 16000889. doi:10.3402/tellusb.v66.22486.

Lopez-Coto, I., S. Ghosh, K. Prasad and J. Whetstone. *Tower-based greenhouse gas mea-surement network design—the national institute of standards and technology north east corridor testbed.* Advances in Atmospheric Sciences, volume 34, no. 9; pages 1095–1105, 2017. ISSN 02561530. doi:10.1007/s00376-017-6094-6.

Mckain, K., A. Down, S. M. Raciti, J. Budney, L. R. Hutyra, C. Floerchinger, S. C. Hern-don, T. Nehrkorn, M. S. Zahniser, R. B. Jackson, N. Phillips and S. C. Wofsy. *Methane emissions from natural gas infrastructure and use in the urban region of boston , mas-sachusetts.* Proceedings of the National Academy of Sciences, volume 112, no. 7, 2015. doi:10.1073/pnas.1416261112.

McKain, K., S. C. Wofsy, T. Nehrkorn, J. Eluszkiewicz, J. R. Ehleringer and B. B. Stephens. *Assessment of ground-based atmospheric observations for verification of greenhouse gas emissions from an urban region.* Proceedings of the National Academy of Sciences, volume 109, no. 22; pages 8423–8428, 2012. ISSN 0027-8424. doi:10.1073/pnas.1116645109.

Mead, M. I., O. A. Popoola, G. B. Stewart, P. Landshoff, M. Calleja, M. Hayes, J. J. Baldovi, M. W. McLeod, T. F. Hodgson, J. Dicks, A. Lewis, J. Cohen, R. Baron, J. R. Saffell and R. L. Jones. *The use of electrochemical sensors for monitoring urban air quality in low-cost, high-density networks.* Atmospheric Environment, volume 70; pages 186–203, 2013. ISSN 13522310. doi:10.1016/j.atmosenv.2012.11.060.

Miller, J. B., S. J. Lehman, S. A. Montzka, C. Sweeney, B. R. Miller, A. Karion, C. Wolak, E. J. Dlugokencky, J. Southon, J. C. Turnbull and P. P. Tans. *Linking emissions of fossil fuel co2 and other anthropogenic trace gases using atmospheric 14co2.* Journal of Geophysical Research: Atmospheres, volume 117, 2012. doi:10.1029/2011JD017048.

Mitchell, L. E., E. T. Crosman, A. A. Jacques, B. Fasoli, L. Leclair-Marzolf, J. Horel, D. R. Bowling, J. R. Ehleringer and J. C. Lin. *Monitoring of greenhouse gases and pollutants across an urban area using a light-rail public transit platform.* Atmospheric Environment, volume 187, no. December 2017; pages 9–23, 2018a. ISSN 18732844. doi: 10.1016/j.atmosenv.2018.05.044.

Mitchell, L. E., J. C. Lin, D. R. Bowling, D. E. Pataki, C. Strong, A. J. Schauer, R. Bares, S. E. Bush, B. B. Stephens, D. Mendoza, D. Mallia, L. Holland, K. R. Gurney and J. R. Ehleringer. *Long-term urban carbon dioxide observations reveal spatial and temporal dynamics related to urban characteristics and growth.* Proceedings of the National Academy of Sciences, volume 115, no. 12; pages 2912–2917, 2018b. ISSN 0027-8424. doi: 10.1073/pnas.1702393115.

Moltchanov, S., I. Levy, Y. Etzion, U. Lerner, D. M. Broday and B. Fishbain. *On the feasibility of measuring urban air pollution by wireless distributed sensor networks.* Science of the Total Environment, The, volume 502; pages 537–547, 2015. ISSN 0048-9697. doi: 10.1016/j.scitotenv.2014.09.059.

Mueller, M., J. Meyer and C. Hueglin. *Design of an ozone and nitrogen dioxide sensor unit and its long-term operation within a sensor network in the city of zurich.* Atmospheric Measurement Techniques, volume 10, no. 10; pages 3783–3799, October 2017. doi:10.5194/amt-10-3783-2017.

Müller, M., P. Graf, J. Meyer, A. Pentina, D. Brunner, F. Perez-Cruz, C. Hüglin and L. Emmenegger. *Integration and calibration of non-dispersive infrared (ndir) co2 low-cost sensors and their operation in a sensor network covering switzerland.* Atmospheric Measurement Techniques, volume 13, no. 7; pages 3815–3834, 2020. ISSN 18678548. doi: 10.5194/amt-13-3815-2020.

Nassar, R., T. G. Hill, C. A. McLinden, D. Wunch, D. B. Jones and D. Crisp. *Quantifying co2 emissions from individual power plants from space.* Geophysical Research Letters, volume 44, no. 19; pages 10,045–10,053, 2017. ISSN 19448007. doi:10.1002/2017GL074702.

Nathan, B., T. Lauvaux, J. C. Turnbull and K. R. Gurney. *Investigations into the use of multi-species measurements for source apportionment of the indianapolis fossil fuel co2 signal.* Elementa, volume 6, no. 2016, 2018. ISSN 23251026. doi:10.1525/elementa.131.

Newman, S., S. Jeong, M. L. Fischer, X. Xu, C. L. Haman, B. Lefer, S. Alvarez, B. Rappenglueck, E. A. Kort, A. E. Andrews, J. Peischl, K. R. Gurney, C. E. Miller and Y. L.

Yung. *Diurnal tracking of anthropogenic CO2 emissions in the los angeles megacity during spring 2010.* Atmospheric Chemistry and Physics, volume 13, no. 8; pages 4359–4372, April 2013. doi:10.5194/acp-13-4359-2013.

Newman, S., X. Xu, K. R. Gurney, Y. K. Hsu, K. F. Li, X. Jiang, R. Keeling, S. Feng, D. O'Keefe, R. Patarasuk, K. W. Wong, P. Rao, M. L. Fischer and Y. L. Yung. *Toward consistency between trends in bottom-up co2 emissions and top-down atmospheric measurements in the los angeles megacity.* Atmospheric Chemistry and Physics, volume 16, no. 6; pages 3843–3863, 2016. ISSN 16807324. doi:10.5194/acp-16-3843-2016.

Papapostolou, V., H. Zhang, B. J. Feenstra and A. Polidori. *Development of an environmental chamber for evaluating the performance of low-cost air quality sensors under controlled conditions.* Atmospheric Environment, volume 171; pages 82–90, 2017. ISSN 1352-2310. doi:10.1016/j.atmosenv.2017.10.003.

Park, S. S., A. Vijayan, S. L. Mara and J. D. Herner. *Investigating the real-world emission characteristics of light-duty gasoline vehicles and their relationship to local socioeconomic conditions in three communities in los angeles, california.* Journal of the Air and Waste Management Association, 2016. ISSN 21622906. doi:10.1080/10962247.2016.1197166.

Pataki, D. E., D. R. Bowling and J. R. Ehleringer. *Seasonal cycle of carbon dioxide and its isotopic composition in an urban atmosphere : Anthropogenic and biogenic effects.* Journal of Geophysical Research, volume 108; pages 1–8, 2003. doi:10.1029/2003JD003865.

Pataki, D. E., D. R. Bowling, J. R. Ehleringer and J. M. Zobitz. *High resolution atmospheric monitoring of urban carbon dioxide sources.* Geophysical Research Letters, volume 33, no. September 2005; pages 1–5, 2006. doi:10.1029/2005GL024822.

Pataki, D. E., B. J. Tyler, R. E. Peterson, A. P. Nair, W. J. Steenburgh and E. R. Pardyjak. *Can carbon dioxide be used as a tracer of urban atmospheric transport ?* Journal of Geophysical Research, volume 110; pages 1–8, 2005. doi:10.1029/2004JD005723.

Patarasuk, R., K. R. Gurney, D. O. Keeffe, Y. Song, J. Huang, P. Rao, M. Buchert, J. C. Lin, D. Mendoza and J. R. Ehleringer. *Urban high-resolution fossil fuel co2 emissions quantification and exploration of emission drivers for potential policy applications.* Urban Ecosystems, volume 19, 2016. doi:10.1007/s11252-016-0553-1.

Piedrahita, R., Y. Xiang, N. Masson, J. Ortega, A. Collier, Y. Jiang, K. Li, R. P. Dick, Q. Lv and M. Hannigan. *The next generation of low-cost personal air quality sensors for quantitative exposure monitoring.* Atmospheric Measurement Techniques, volume 3, no. 2; pages 3325–3336, 2014. doi:10.5194/amt-7-3325-2014.

Sadighi, K., E. Coffey, A. Polidori, B. Feenstra, Q. Lv, D. K. Henze and M. Hannigan. *Intra-urban spatial variability of surface ozone in riverside, CA: viability and validation of low-cost sensors.* Atmospheric Measurement Techniques, volume 11, no. 3; pages 1777–1792, March 2018. doi:10.5194/amt-11-1777-2018.

Sargent, M., Y. Barrera, T. Nehrkorn, L. R. Hutyra, C. K. Gately, T. Jones, K. McKain, C. Sweeney, J. Hegarty, B. Hardiman and S. C. Wofsy. *Anthropogenic and biogenic co2 fluxes in the boston urban region.* Proceedings of the National Academy of Sciences, volume 115, no. 29; pages 7491–7496, 2018. ISSN 0027-8424. doi:10.1073/pnas.1803715115.

Shusterman, A. A., J. Kim, K. J. Lieschke, C. Newman, P. J. Wooldridge and R. C. Cohen. *Observing local co2 sources using low-cost, near-surface urban monitors.* Atmospheric Chemistry and Physics, volume 18, no. 18; pages 13 773–13 785, 2018. ISSN 16807324. doi:10.5194/acp-18-13773-2018.

Shusterman, A. A., V. E. Teige, A. J. Turner, C. Newman, J. Kim and R. C. Cohen. *The BErkeley atmospheric co2 observation network: initial evaluation.* Atmospheric Chemistry and Physics, volume 16, no. 21; pages 13 449–13 463, October 2016. doi:10.5194/acp-16-13449-2016.

Staufer, J., G. Broquet, F.-M. Bréon, V. Puygrenier, F. Chevallier, I. Xueref-Rémy, E. Dieudonné, M. Lopez, M. Schmidt, M. Ramonet, O. Perrussel, C. Lac, L. Wu and P. Ciais. *The first 1-year-long estimate of the paris region fossil fuel co2 emissions based on atmospheric inversion.* Atmospheric Chemistry and Physics, volume 16, no. 22; pages 14 703–14 726, November 2016. doi:10.5194/acp-16-14703-2016.

Sun, L., K. C. Wong, P. Wei, S. Ye, H. Huang and F. Yang. *Development and application of a next generation air sensor network for the hong kong marathon 2015 air quality monitoring.* Sensors, volume 16, no. 211, 2015. doi:10.3390/s16020211.

Super, I., H. A. Van Der Gon, M. K. Van Der Molen, H. A. Sterk, A. Hensen and W. Peters. *A multi-model approach to monitor emissions of co2 and co from an urban-industrial complex.* Atmospheric Chemistry and Physics, volume 17, no. 21; pages 13 297–13 316, 2017a. ISSN 16807324. doi:10.5194/acp-17-13297-2017.

Super, I., H. A. Van Der Gon, A. Visschedijk, M. Moerman, H. Chen, M. K. Van Der Molen and W. Peters. *Interpreting continuous in-situ observations of carbon dioxide and carbon monoxide in the urban port area of rotterdam.* Atmospheric Pollution Research, volume 8, no. 1; pages 174–187, 2017b. ISSN 1309-1042. doi:10.1016/j.apr.2016.08.008.

Turnbull, J. C., A. Karion, M. L. Fischer, I. Faloona, T. Guilderson, S. J. Lehman, B. R. Miller, J. B. Miller, S. Montzka, T. Sherwood, S. Saripalli, C. Sweeney and P. P. Tans. *Assessment of fossil fuel carbon dioxide and other anthropogenic trace gas emissions from airborne measurements over sacramento, california in spring 2009.* Atmospheric Chemistry and Physics, volume 11, no. 2; pages 705–721, January 2011. doi:10.5194/acp-11-705-2011.

Turnbull, J. C., J. B. Miller, S. J. Lehman, P. P. Tans, R. J. Sparks and J. Southon. *Comparison of 14 co2, co, and sf6 as tracers for recently added fossil fuel co2 in the atmosphere and implications for biological co2 exchange.* Geophysical Research Letters, volume 33; pages 2–6, 2006. doi:10.1029/2005GL024213.

Turnbull, J. C., C. Sweeney, A. Karion, T. Newberger, S. J. Lehman, P. P. Tans, K. J. Davis, T. Lauvaux, N. L. Miles, S. J. Richardson, M. O. Cambaliza, P. B. Shepson, K. R. Gurney, R. Patarasuk and I. Razlivanov. *Toward quantification and source sector identification of fossil fuel co2 emissions from an urban area: Results from the influx experiment.* Journal of Geophysical Research, volume 120, no. 1; pages 292–312, 2015. ISSN 21562202. doi: 10.1002/2014JD022555.

Turner, A. J., J. Kim, H. Fitzmaurice, C. Newman, K. Worthington, K. Chan, P. J. Wooldridge, P. Köehler, C. Frankenberg and R. C. Cohen. *Observed impacts of COVID-19 on urban CO2 emissions.* Geophysical Research Letters, volume 47, no. 22, November 2020a. doi:10.1029/2020gl090037.

Turner, A. J., P. Köhler, T. S. Magney, C. Frankenberg, I. Fung and R. C. Cohen. *A double peak in the seasonality of california's photosynthesis as observed from space.* Biogeosciences, volume 17, no. 2; pages 405–422, January 2020b. doi:10.5194/bg-17-405-2020.

Turner, A. J., A. A. Shusterman, B. C. Mcdonald, V. Teige, R. A. Harley and R. C. Cohen. *Network design for quantifying urban co2 emissions: assessing trade-offs between precision and network density.* Atmospheric Chemistry and Physics, (pages 13 465–13 475), 2016. doi:10.5194/acp-16-13465-2016.

Varon, D. J., D. J. Jacob, J. McKeever, D. Jervis, B. O. A. Durak, Y. Xia and Y. Huang. *Quantifying methane point sources from fine-scale satellite observations of atmospheric methane plumes.* Atmospheric Measurement Techniques, volume 11, no. 10; pages 5673–5686, October 2018. doi:10.5194/amt-11-5673-2018.

Verhulst, K. R., A. Karion, J. Kim, P. K. Salameh, R. F. Keeling, S. Newman, J. B. Miller, C. Sloop, T. Pongetti, P. Rao, C. Wong, F. M. Hopkins, V. Yadav, R. F. Weiss, R. M. Duren and C. E. Miller. *Carbon dioxide and methane measurements from the los angeles megacity carbon project - part 1: Calibration, urban enhancements, and uncertainty estimates.* Atmospheric Chemistry and Physics, volume 17, no. 13; pages 8313–8341, 2017. ISSN 16807324. doi:10.5194/acp-17-8313-2017.

Viatte, C., T. Lauvaux, J. K. Hedelius, H. Parker, J. Chen, T. Jones, J. E. Franklin, A. J. Deng, B. Gaudet, K. Verhulst, R. Duren, D. Wunch, C. Roehl, M. K. Dubey, S. C. Wofsy and P. O. Wennberg. *Methane emissions from dairies in the los angeles basin.* Atmospheric Chemistry and Physics, volume 17, no. 12; pages 7509–7528, 2017. ISSN 16807324. doi:10.5194/acp-17-7509-2017.

Vogel, F. R., M. Frey, J. Staufer, F. Hase, G. Broquet and I. Xueref-remy. *Xco2 in an emission hot-spot region : the coccon paris campaign 2015.* Atmospheric Chemistry and Physics, volume 19; pages 3271–3285, 2019.

Waxman, E. M., K. C. Cossel, F. Giorgetta, G.-W. Truong, W. C. Swann, I. Coddington and N. R. Newbury. *Estimating vehicle carbon dioxide emissions from boulder, colorado, using*

horizontal path-integrated column measurements. Atmospheric Chemistry and Physics, volume 19, no. 7; pages 4177–4192, April 2019. doi:10.5194/acp-19-4177-2019.

Williams, D. E., G. S. Henshaw, M. Bart, G. Laing, J. Wagner, S. Naisbitt and J. A. Salmond. *Validation of low-cost ozone measurement instruments suitable for use in an air-quality monitoring network.* Measurement Science and Technology, volume 24, 2013. doi:10.1088/0957-0233/24/6/065803.

Wong, C., D. Fu, T. J. Pongetti, S. Newman, E. A. Kort, R. M. Duren, Y. K. Hsu, C. E. Miller, Y. L. Yung and S. P. Sander. *Mapping ch4 : Co2 ratios in los angeles with clars-fts from mount wilson, california.* Atmospheric Chemistry and Physics, volume 15, no. 1; pages 241–252, 2015. ISSN 16807324. doi:10.5194/acp-15-241-2015.

Wu, K., T. Lauvaux, K. J. Davis, A. Deng, I. L. Coto, K. R. Gurney and R. Patarasuk. *Joint inverse estimation of fossil fuel and biogenic co2 fluxes in an urban environment: An observing system simulation experiment to assess the impact of multiple uncertainties.* Elementa, volume 6, no. February, 2018. ISSN 23251026. doi:10.1525/elementa.138.